SAND REPORT

SAND2002-1369
Unlimited Release
Printed May 2002

Field Investigation of Flow Processes Associated with Infiltration into an Initially Dry Fracture Network at Fran Ridge, Yucca Mountain, Nevada: A Photo Essay and Data Summary

Michael J. Nicholl and Robert J. Glass

Prepared by
Sandia National Laboratories
Albuquerque, New Mexico 87185 and Livermore, California 94550

Sandia is a multiprogram laboratory operated by Sandia Corporation, a Lockheed Martin Company, for the United States Department of Energy under Contract DE-AC04-94AL85000.

Sandia National Laboratories

Issued by Sandia National Laboratories, operated for the United States Department of Energy by Sandia Corporation.

Available to DOE and DOE contractors from
U.S. Department of Energy
Office of Scientific and Technical Information
P.O. Box 62
Oak Ridge, TN 37831

Telephone: (865)576-8401
Facsimile: (865)576-5728
E-Mail: reports@adonis.osti.gov
Online ordering: http://www.doe.gov/bridge

Available to the public from
U.S. Department of Commerce
National Technical Information Service
5285 Port Royal Rd
Springfield, VA 22161

Telephone: (800)553-6847
Facsimile: (703)605-6900
E-Mail: orders@ntis.fedworld.gov
Online order: http://www.ntis.gov/ordering.htm

SAND*2002-1369*
Unlimited Release
Printed May 2002

Field Investigation of Flow Processes Associated with Infiltration into an Initially Dry Fracture Network at Fran Ridge, Yucca Mountain, Nevada: A Photo Essay and Data Summary

Michael J. Nicholl
Department of Materials, Metallurgical, Mining and Geological Engineering
University of Idaho
Moscow, ID 83844-3024
Email: mnicholl@uidaho.edu

Robert J. Glass
Geohydrology Department, Flow Visualization and Processes Laboratory
Sandia National Laboratories
P.O. Box 5800
Albuquerque, NM 87185-0735
Email: rjglass@sandia.gov

Abstract

This photo essay introduces a unique field investigation specifically designed to enhance our understanding of flow processes in unsaturated fractured rock. We infiltrated dyed water into an initially dry fracture network located on Fran Ridge, near Yucca Mountain, Nevada. Later, the rock mass beneath our infiltration sites was excavated to a depth of ~5m in a series of horizontal layers (~0.5 m thick); at each stage of the excavation process, we recorded portions of the fracture network marked with the dye tracer. The goals of this investigation were to: 1) obtain fracture network data from the Topopah Spring Tuff unit for use in intermediate-scale simulations; 2) identify portions of the fracture network conducting flow under three different boundary conditions; 3) visualize preferential flow paths and small-scale flow structures; 4) collect samples for subsequent hydraulic testing and use in intermediate-scale simulations; and 5) demonstrate the utility of Electrical Resistance Tomography (ERT) to delineate fluid distribution within fractured rock. Here, we document this unique investigation with a series of captioned photographs, drawings, and plots of measured data. Results of this experiment highlight the extreme complexity of flow processes in unsaturated fractured rock, and the resulting difficulty of both predicting and monitoring such flows.

Preface

At this time, very little experimental evidence exists regarding the fundamental processes of flow and transport through unsaturated, fractured rock. While a small number of investigators are working at the laboratory scale, well designed field experiments are scarce. Due to the extreme difficulty and expense of conducting such experiments, most field tests have been designed to obtain property values for use in existing conceptual models, rather than to develop improved understanding and new conceptual models. In 1994, we conducted a unique field investigation specifically designed to enhance our understanding of flow processes in unsaturated fractured rock [Nicholl and Glass, 1995]. The goals of this investigation were to: 1) obtain fracture network data from the Topopah Spring Tuff unit for use in intermediate-scale simulations; 2) identify portions of the fracture network conducting flow under three different boundary conditions; 3) visualize preferential flow paths and small-scale flow structures; 4) collect samples for subsequent hydraulic testing and use in intermediate-scale simulations; and 5) demonstrate the utility of Electrical Resistance Tomography (ERT) to delineate fluid distribution within fractured rock.

Although interpretation of this test is being published elsewhere [Glass et al., 2002], other investigators have suggested that the scientific community would benefit from a photo-essay describing the investigation, and documenting key observations. Use of electronic media allows us to provide more images than would be feasible with conventional print media, and many more than would be possible for journal publication. It also allows us to disseminate raw and reduced data in a form usable to other investigators. We begin this electronic document with a concise overview of the investigation, and then present a series of captioned figures that are organized by topic. The CD-ROM version of this document also includes folders containing full resolution copies of the figure images and data collected during the experiment; use of these images and data is welcomed, provided that the origin is properly cited.

Navigating this Document

Figures

The bulk of this document consists of a set of captioned figures documenting our investigation. Figures are categorized by topic; the opening page of each topic contains a short overview of the included material.

Important notes:

1) Two versions of the principal document are provided. The only difference between the two versions is image resolution. The file containing the high resolution version (FRAN_H.PDF) is much larger (~51 megabytes) then the file containing the low resolution version (FRAN_L.PDF, ~9 megabytes).

2) At first glance, some of the photographs on the high-resolution version of this document (FRAN_H.PDF) will appear to be grainy or flat (low contrast) when viewed on screen. This is a screen resolution issue; each of the photographic images has been inserted into the PDF document at 300 DPI resolution, so **please zoom in** and take a closer look. Images will be somewhat more grainy on the low-resolution version (FRAN_L.PDF).

3) A "return" button is located in the upper left corner of each figure page. Unlike internet browsers, this button returns to the previous view, rather than the previous page. Therefore, if you have zoomed into the image, multiple clicks on the return button may be required to get back to the previous page.

4) Blue text within the figure captions is linked to the referenced pages. A single click on the blue text will activate the link.

Table of Contents

1. Overview of the Investigation
2. Experimental Site
3. Ponded Infiltration Experiment
4. Excavation and Mapping
5. Mapping Results (ponded test)
6. Images Denoting Maximum Tracer Extent (ponded test)
7. Local Flow Features
8. Rock Mass Variability
9. Acknowledgements
10. Guide to Appendices
11. Reference List
12. Distribution List

Section 1 - Overview of the Investigation

Our investigation was performed in conjunction with construction activities associated with the Large Block Test (LBT), a scientific investigation conducted by Lawrence Livermore National Laboratory (LLNL). Preparation for the LBT required that a test block (4.5 x 3 x 3 m) be carefully excavated from an outcrop of nonlithophysal Topopah Spring tuff located on the eastern slope of Fran Ridge near Yucca Mountain, Nevada [see Lin et al., 1994; Wilder et al., 1997; Lin et al., 2001]. In essence, the construction plan was to define a block within the rock mass, and then remove the waste material surrounding it. This unusual procedure provided us with a unique opportunity to conduct simple field experiments exploring flow structure in an initially dry fracture network.

Excavation of the LLNL Large Block began by benching the hillside to create a level work area (~12 x 12 m in plan) at a depth of 1-3 m below surface; a vertical face was also cut on the downslope side of the excavation. Near the center of this work area, a belt saw was used to cut four vertical slots (4.5 m deep). The slots were arranged in a square to isolate a 3 x 3 m (plan) section of the rock mass from the rest of the formation. The 3 x 3 x 4.5 m Large Block was then exhumed by removing the surrounding rock in a series of roughly horizontal lifts (vertical intervals of ~0.5 m).

Our investigation began at an intermediate stage of excavation; after the vertical slots were cut, and prior to removing rock surrounding the Large Block. At three different locations, we infiltrated fluid containing a visible tracer into fractures within the rock mass adjoining the Large Block. We then recorded observations while the rock beneath those experiments was excavated. The fracture network and distribution of the visible tracer were mapped over a series of horizontal pavements immediately below the infiltration surfaces. Our principal goal was to explore flow structure within the fracture network beneath a surface pond; hence, most of this document focuses on one of the three experiments (hereafter referred to as the Ponded Infiltration Test). In order to guide future work, we also performed two ancillary experiments designed to induce unsaturated conditions near to the infiltration surface; a lesser number of observations from the Restricted Flow Test and the Small Slug Test will be reported.

1.1 - Ponded infiltration test

A ~6 m^2 (8 x 8’) location in the southwest corner of the area leveled for the Large Block Test was selected for this experiment. Visual inspection of the pavement and excavation walls at this location suggested that the extremely tight matrix would confine flow to the pervasive (< 30 cm spacing) fracture network. In addition, exposed fractures showed relatively small amounts of secondary mineralization (e.g., coating, filling). Dry initial conditions were assumed for the fracture network, as potential evapotranspiration in this region (125-200+ cm/year) greatly exceeds annual rainfall (8-10 cm/year) [Bedinger et al., 1990]. Following site selection, a shallow (~0.2 m) infiltration pond (~3.5 m^2 surface area) was excavated into the rock surface. A geophysical array was also installed (see next page) to test the utility of Electrical Resistance Tomography (ERT) for detecting water content changes within the network.

The ponded infiltration test was initiated by pouring ~150 liters of fluid into the pond from buckets. At the same time, gravity flow was induced from a tank located several meters above the infiltration pond; outflow from the tank was monitored at 10 second intervals using a pair of calibrated pressure transducers. Fluid level in the pond was controlled by a float valve. Pond level stabilized ~10 minutes after initial addition of fluid; after that time, outflow from the supply tank is expected to equal infiltration into the fracture network. Measured flow from the feed tank (~640 liters) ended after ~36 minutes, for a total infiltration volume of ~790 liters. The infiltrating fluid consisted of local well water (J13), with blue food coloring (FD&C Blue #1) added (~4 g/l) as a visible tracer consistent with environmental mandates.

1.2 - Electrical Resistance Tomography of the Ponded Infiltration Test

Investigators from LLNL explored the utility of Electrical Resistance Tomography (ERT) for detecting water content changes in a fracture network by measuring resistivity over a set of two-dimensional vertical planes beneath the infiltration pond before, during, and after infiltration. Four ERT strings, each 3 m long and containing 11 electrodes (30 cm apart) were grouted into dry drilled vertical holes located within the pond at the corners of a 1.5 x 1.5 m square. Installation was designed to minimize perturbations to the system, provide electrical contact with the rock mass, inhibit the formation of preferential pathways, and maximize coverage across the primary vertical fracture sets. Eight shallow (~15 cm) surface electrodes were installed along diagonals of the square to increase resolution in those planes.

Test design was to bring infiltration to steady state, and then collect a full suite of ERT data (i.e., between all string pairs). It was presumed that during steady infiltration, fluid geometry within the interrogated zone would remain unchanged over the time required to obtain a full set of ERT data (10-20 minutes); thus providing optimal conditions for assessing the ability of ERT to discern moisture distribution within the fracture network. Ground truth for assessing the ERT results would come from maps of the fracture network and tracer distribution made during subsequent excavation of the site. Test design also included acquisition of transient ERT data across one of the primary planes during infiltration and subsequent drainage.

Unfortunately, the unexpectedly high infiltration rate shortened the duration of the test; hence, measurements during infiltration were limited to two sequential cross-hole ERT resistance fields in a single plane. The full suite of measurements (i.e., resistivity fields between all string pairs) were measured on the day before the test, over the hour following infiltration, and on the next day. Unfortunately, due to budgetary constraints, ERT data was only reduced in a preliminary fashion, as can be found in archived scientific notebooks [LLNL YMP controlled scientific notebook LBT-03, 3/4/94, pp. 5-26].

1.3 - Ancillary tests

As described above, our primary purpose was to investigate phase structure in a natural fracture network beneath a surface pond. However, we also attempted two additional infiltration tests within the LLNL excavation. The Restricted Flow Test was performed in the northeast corner of the excavation. Fine sand tamped into the infiltration pond was expected to restrict flow into the network, creating unsaturated flow conditions near the pond. This test failed during infiltration, when flow short-circuited the pond through a shallow subhorizontal fracture and rapidly appeared elsewhere at the ground surface. In the northwest corner of the excavation, a small fluid slug (~20 liters) was applied to the network (Small Slug Test). Unfortunately, infiltration rate was dramatically reduced due fracture infilling by secondary mineralization; hence a significant amount of the slug was lost to evaporation. Even though these two tests were located within 15 m of our primary test, material properties differed sufficiently to preclude direct comparisons. However, we did note interesting flow features associated with these two sites, which will be reported with our general observations of flow structure.

1.4 - Excavation and mapping

Waste rock surrounding the LLNL Large Block (including the region of our tests) was removed in a series of roughly horizontal lifts. At each level, the exposed rock pavement was broken to a depth of ~0.5 m with a large vehicle-mounted jackhammer. A buffer zone of approximately 1 m was maintained to protect the LLNL Large Block during this concussive excavation. Later in the excavation process, large samples were extracted from the buffer zone for use in the LLNL investigation. At each excavation level, most of the waste rock was removed with a small bulldozer. The pavement was then cleaned to bare rock over a ~6 m^2 (8 x 8’) area directly below each infiltration site. Large rocks were moved by hand, and fine debris was blown away with pressurized air. The fracture network and tracer distributions were mapped at the infiltration surface and each subsequent excavation level; there were a total of 12 levels for the ponded infiltration test (0-11), 8 for the restricted flow test (0-7), and 7 for the small slug test (0-6).

At each new level, fracture traces and dye stains were recorded at a scale of 1:12 by hand mapping. A portable 2.44 x 2.44 m (8 x 8’) grid subdivided at 0.305 x 0.305 m (1 x 1’) intervals was used as a reference. Mapping was performed shortly after the pavement was cleaned in order to maximize visibility of the dye tracer. In the short term, construction dust rapidly settled on exposed surfaces and obscured the tracer. Over a much longer term than we allowed the pavements to remain exposed (several hours), the dye we used would likely suffer partial degradation from exposure to ultraviolet radiation. The longest fracture traces were mapped first, and then successively smaller features as time allowed. Wherever possible, the dip of individual fractures was measured (+/- 5°) on exposed surfaces. During excavation, we also noted the approximate location and extent of tracer encountered outside of the mapped area on the excavation walls, and in the excavated rubble.

The delay between infiltration and excavation provided sufficient time for fluid to escape the near-surface network (drainage, imbibition, evaporation), thereby precluding remobilization of the tracer during excavation. However, the nature of the excavation process, which was designed specifically for the LLNL investigation, did place the following constraints on our mapping process. 1) Interval between pavements was not consistent. 2) Roughness and dip of the mapped area varied considerably. 3) Only a small area was cleared to bare rock, hence we were unable to obtain a detailed record of tracer migration outside of the mapped area. 4) Excavation was restricted to horizontal pavements; therefore we could not explore evidence of flow mechanisms in the plane of inclined fractures (e.g., gravity driven fingering) except through observation of broken blocks. 5) Time constraints were imposed by the excavation schedule; mapping activities were performed immediately after a lift was cleaned, and in the shortest possible time. As a result, maps taken at levels 7, 9, and 10 contain less detail than those at other levels. 6) Excavation stopped at a depth of ~5 m, while the infiltration pulse clearly penetrated below this depth.

Section 2 - Experimental Site

Images in this section show the location of the test, plan map of the excavation, and site preparation.

return

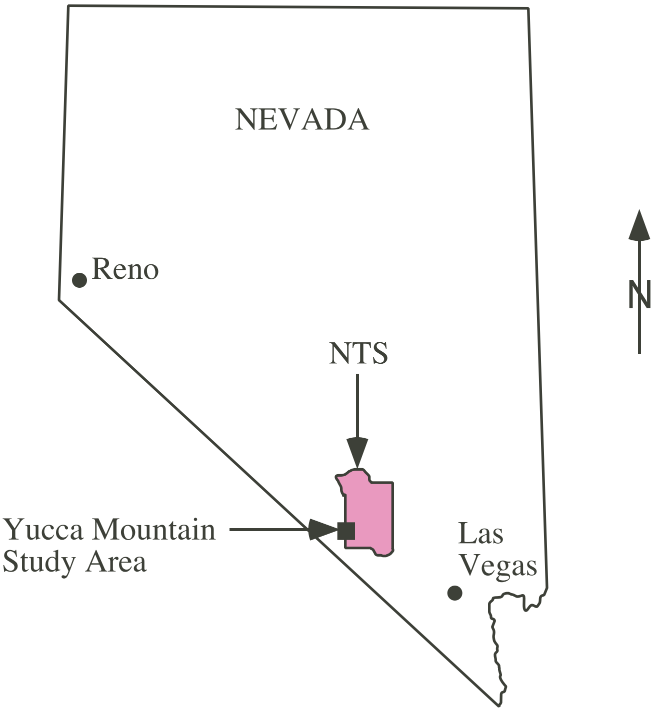

Figure 2.1 - location map: Our investigation was conducted at a site located on the eastern side of Fran Ridge. This low (~1300 m above MSL) north-south trending ridge is situated near the western edge of the Nevada Test Site (NTS) in Nye County, Nevada. With respect to local topographic features (see figures 2.2 – Yucca Mountain aerial view, and 2.3 - Yucca Mountain satellite image), Fran Ridge is located roughly parallel to, and slightly east of Yucca Mountain, west of 40 Mile Wash and Jackass Flats, north of Busted Butte, and southwest of the Calico Hills and Shoshone Mountain (~1910 m above MSL). The work site (see figure 2.4 - site on Fran Ridge) was located at approximately N748500, E574500 on the Busted Butte Quadrangle [USGS, 1983].

Nicholl and Glass, 2002

return

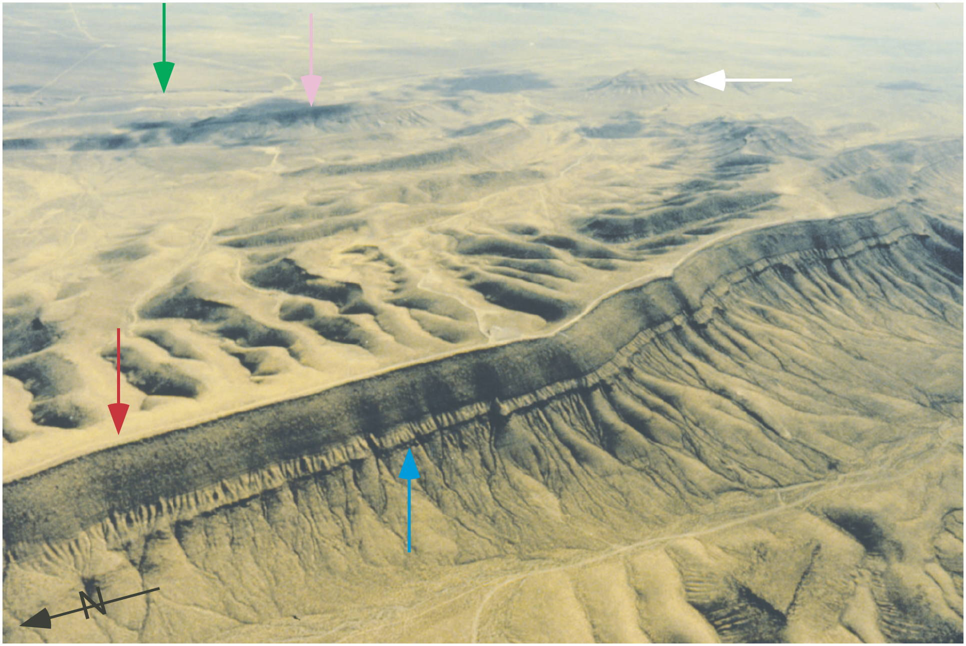

Figure 2.2 - Yucca Mountain aerial view: Oblique aerial view looking generally southeast towards Yucca Mountain (red arrow), Fran Ridge (purple arrow), Busted Butte (white arrow), and 40 Mile Wash (green arrow); Solitario Canyon is in the foreground. The resistant unit standing proud along the west face of Solitario Canyon (blue arrow) is the top of the Topopah Spring Tuff (‘caprock’ and crystal-rich nonlithophysal subunits). Note the access road running along the crest of Yucca mountain. Although difficult to discern in this oblique photograph, Yucca Mountain slopes more steeply to the west (foreground) than it does to the east.

Nicholl and Glass, 2002

return

Figure 2.3 – Yucca Mountain satellite image: This image shows the general relationship between our study site on Fran Ridge and other local features, both topographic and anthropogenic. Satellite image data was obtained from LandSat TM (4,2,1 band), Space Imaging EOSAT, July 24, 1995; approximately one year after completion of our experiment. The base image seen to the right was cropped from a map compiled by Rager [1997]. The white arrow points to the northern end of the road running along the Yucca Mountain crest; Solitario Canyon lies immediately to the west. The black arrow points to a box surrounding the road leading up to the LLNL Large Block Test, which was the site of our experiment. Busted Butte lies at the tip of the blue arrow, while the red arrow points to 40 Mile Wash, with its tail lying on Little Skull Mountain. The red circles near the bottom of the image are irrigated fields in the Amargosa valley, the Calico Hills are seen in the upper right hand corner of the image (northeast), and finally, Highway US 95 crosses at the tip of the north arrow.

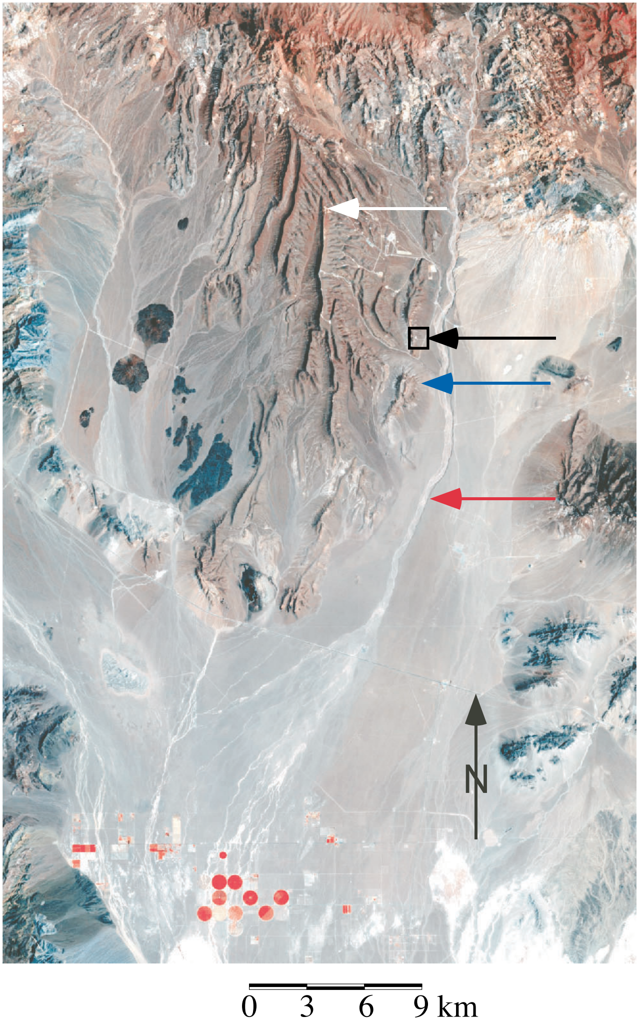

return

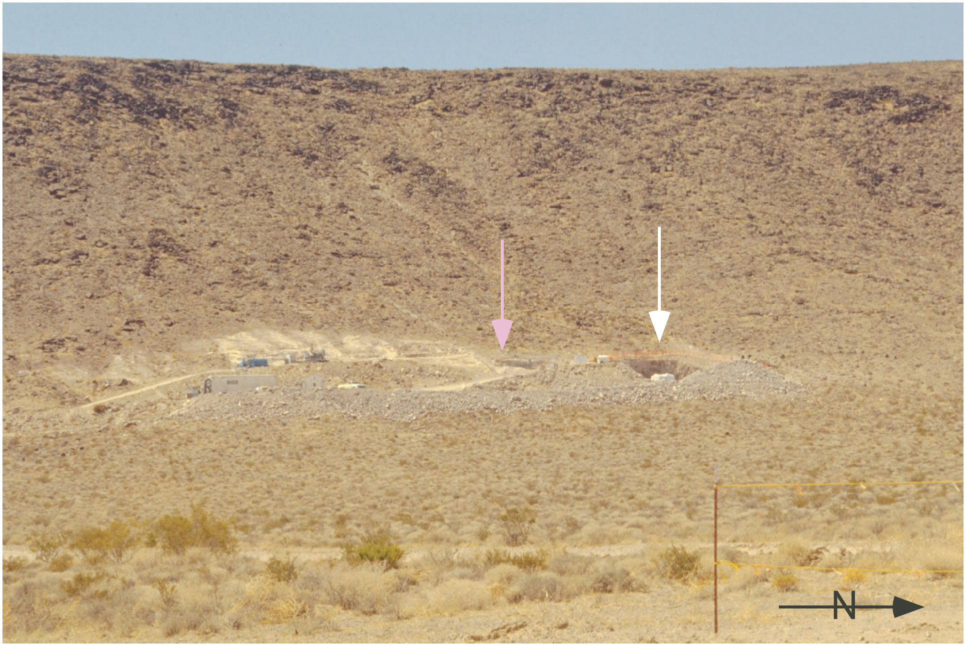

Figure 2.4 - site on Fran Ridge: Work area on Fran Ridge as seen from the east near Forty-Mile Wash; the photograph was taken from near the tip of the black arrow seen in figure 2.3 – Yucca Mountain satellite image. The excavation is located midway up the photograph, and slightly right of center (white arrow). The faint orange band surrounding the excavation is net fencing. The white object in the center of the excavation is the LLNL Large Block, which was wrapped in protective white plastic following exhumation. A water storage tank (also white) is located just outside of the excavation, and to the left. The access road and support equipment (storage trailer, field office, generator, air conditioning unit, etc.) are located left of center (see figure 2.5 - site map). The USGS studied fractures in two pits (~4-5 m deep) and on pavement surfaces (purple arrow) located immediately south and west of the excavation; results are reported in Throckmorton et al. [1995]. Waste from the excavation was placed down slope from the access road, and stretches across most of the image.

Nicholl and Glass, 2002

return

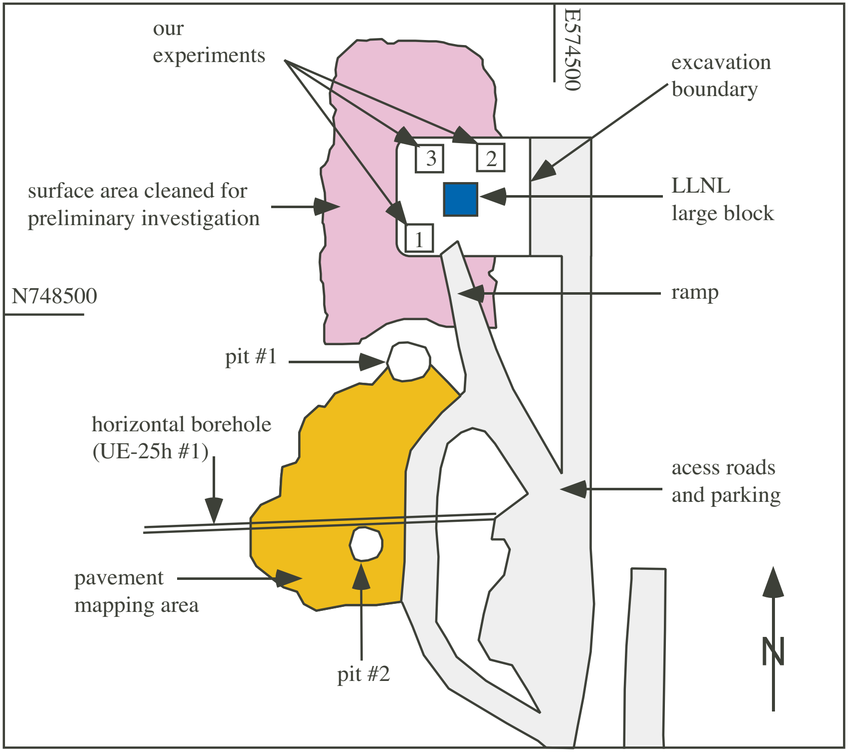

Figure 2.5 - site map: Sketch showing the general site layout with respect to other activities [after Lin et al., 1994]; drawing is not to scale. Yucca Mountain is located directly to the west, and 40 Mile Wash is located to the east. Our experiments (squares numbered 1-3) were performed in the region excavated to expose the LLNL Large Block (see figure 2.4 - site on Fran Ridge). The ponded infiltration test was performed at site 1, the restricted flow test at site 2, and the small slug test at site 3. Fractures exposed on the pavement area, and in pits to the south and west of the excavation were mapped by the USGS [Throckmorton et al., 1995]. The horizontal borehole (UE-25h#1) is described in Norris et al. [1986].

return

Figure 2.6 - work area: Site preparation included excavating a level work area on the side of Fran Ridge. This view looking towards the northwest shows subsequent cutting operations to isolate the LLNL Large Block from the surrounding country rock. Individuals in this image are examining the belt saw (see figure 2.7 - belt saw) employed to cut the vertical slots seen in figure 2.8 - bench face. The saw was moved about the level work area in order to make the requisite number of cuts; four to isolate the LLNL Large Block and a fifth to aid in sampling (see figure 4.7 - excavation in process). Lights placed around the excavation allowed for 24 hour a day operation. The area in shadow on the right side of the image (white arrow) is a vertical face that was excavated to facilitate access (see figure 2.8 - bench face).

return

Figure 2.7 - belt saw: Close-up image of the belt saw used to isolate the LLNL large block from the surrounding country rock (see figure 2.6 - work area). A ~4.4 cm wide diamond encrusted belt rides on a 4.9 meter long bar [Lin, et al., 1994]. The saw travels across the work area on rails (seen on the right hand side of the image), and angle of the blade is controlled hydraulically. The saw cuts were used to define an *in situ* tabular monolith ~4.5 m high and 3 x 3 m in plan for the LLNL investigation. Orange fencing on the left hand side of the image marks the edge of a vertical face excavated into the hillside (see figure 2.8 - bench face). View is to the southeast, looking over Forty Mile Wash and towards Mt. Charleston.

return

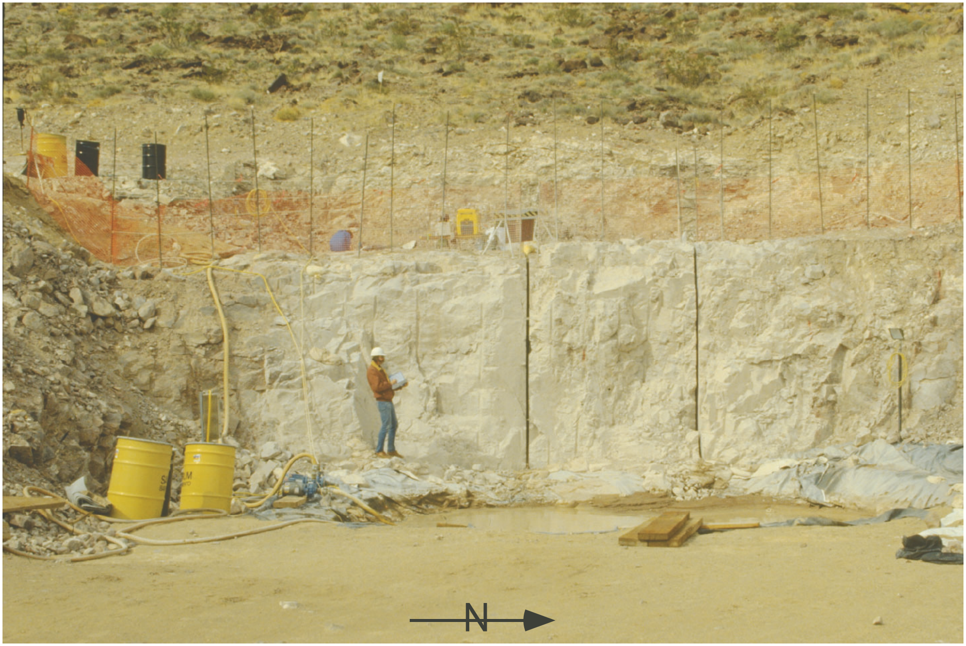

Figure 2.8 - bench face: Site preparations prior to excavation of the LLNL Large Block included benching the side of Fran Ridge to provide access. Looking from the east, the bench face shows two vertical saw cuts created to isolate the Large Block from the surrounding country rock (see figures 2.6 - work area, and 2.7 - belt saw). Cutting fluid (water) was drained away from the bench to the sump seen in the foreground. Barrels in the upper left-hand corner of the image were used to supply fluid for our ponded infiltration test (see figure 3.3 - initiation of flow). M. Mann (SNL) is in front of the bench face (white helmet), directly above him, on the level work area, an individual dressed in blue is preparing for the ponded infiltration test.

Section 3 - Ponded Infiltration Experiment

The primary purpose of this investigation was to investigate flow structure in an initially dry fracture network beneath a surface pond. Images in this section show experimental set-up, infiltration test on 3/11/94, and measurements.

return

Figure 3.1 - infiltration site: In this view looking to the southwest, M. Mann (SNL) is seen preparing for the ponded infiltration test; this view is essentially hidden in the far left hand side of figure 2.6 - work area. Drums on the hillside were used to supply fluid to the test by gravity feed thorough the green hose (see also figure 2.8 – bench face). The infiltration pond (red arrows) was carved into the pavement at a depth of about 3 m below the sloping ground surface. At this depth, the rock was competent and the fracture network was open and mostly unfilled. A close up view of the pond is shown in figure 3.2 - infiltration pond prior to test.

return

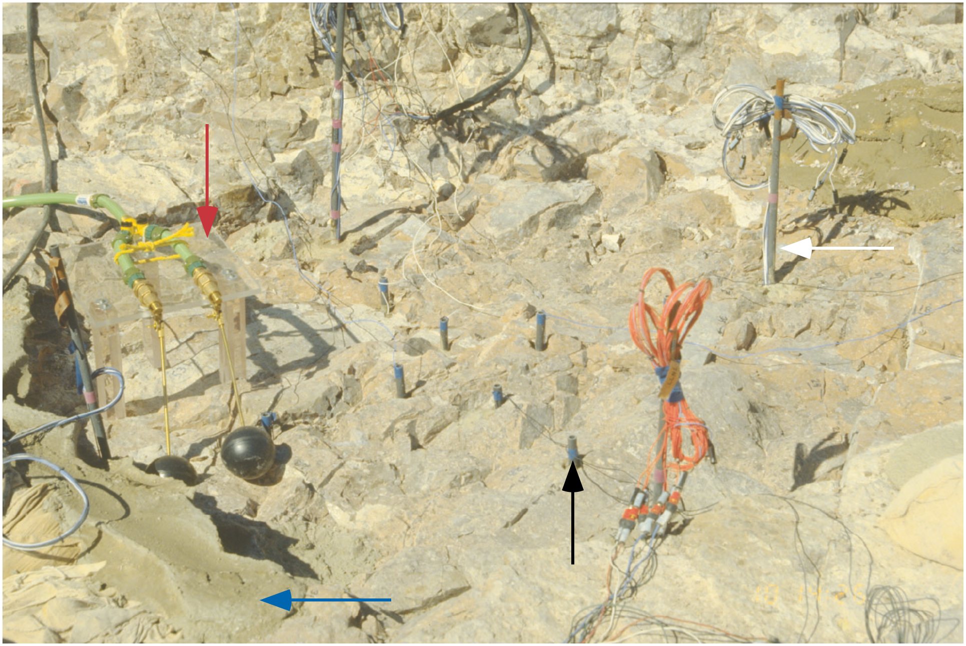

Figure 3.2 - infiltration pond prior to test: Close-up view of the infiltration pond. The excavation method (impact hammer) produced a pond with a very uneven bottom and an irregular outline (see figure 3.8 - ERT array). Concrete (blue arrow) was used to complete the pond in regions where the excavated surface was low. Garden hose (green) connects the fluid supply to paired float valves (black spheres attached to brass rods); support frame for the float valves (red arrow) was made of transparent acrylic, and does not show up well in the image. Geophysical array consisted of four 3 m long ERT strings and eight surface electrodes. The four main ERT strings (taller PVC pipes, one is marked by the white arrow) were placed in a 1.5 x 1.5 m (4.9 x 4.9 ft.)square near the edges of the pond and aligned to image across the primary vertical fracture sets (see figures 3.8 - ERT array and 5.4 fracture orientations). The surface electrodes (shorter PVC pipes, one is marked by the black arrow) were placed along the diagonals of the square.

Nicholl and Glass, 2002

return

Figure 3.3 - initiation of flow: On the morning of 3/11/94, infiltration was started by pouring ~150 liters of fluid into the pond from buckets; at the same time, gravity feed to the float valve was initiated. In this view, looking slightly west of south, B. Daily and A. Ramirez (LLNL) are checking the ERT array; R.J. Glass (SNL) is adjusting the float valve; and M. Mann (SNL) is monitoring the fluid reservoirs and data acquisition system. Tops of the four primary ERT strings can be seen above the pond surface (one is marked by the white arrow). Also, note the two pieces of PVC pipe protruding from the fluid supply drum (red arrow); each pipe held two pressure transducers for monitoring fluid level (see figure 3.5 - infiltration).

return

Figure 3.4 - setting ponded depth: Fluid level in the pond was stabilized ~10 minutes after initial addition of fluid. After setting the pond level, storage in the pond remained constant until fluid addition ceased. Therefore, conservation of mass implies equivalency between outflow from the fluid supply drum and infiltration through the base of the pond. Here, R.J. Glass (SNL) adjusts the float valves used to maintain fluid level; note that he is not wearing blue gloves. Two of the main ERT strings and several of the surface electrodes can also be seen in this image.

return

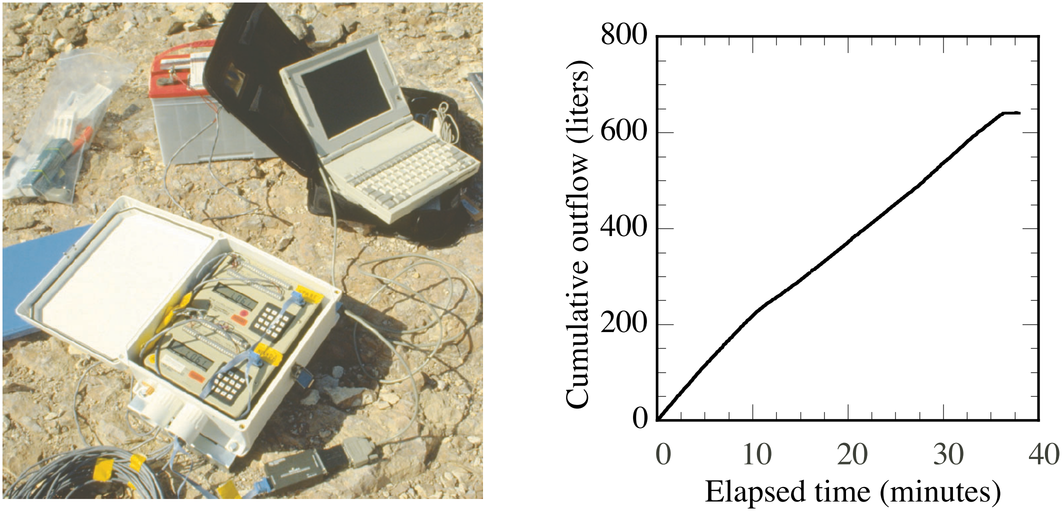

Figure 3.5 - infiltration: Outflow from the fluid supply drum was monitored as an analog for infiltration rate (see figure 3.4 – setting ponded depth). Fluid level in the supply drum was measured at 10 second intervals using two calibrated pressure transducers read by a portable datalogger. A complete backup system (transducers and datalogger) was also employed. Data was downloaded onto a laptop computer immediately following infiltration; an in-line optical interface was used to protect both devices during data transfer. The entire system was powered by a twelve-volt automotive battery. After setting the float valve in the pond ~10 minutes after initiation of the test, outflow from the supply drum (see figure 3.3 - initiation of flow) matches fluid lost to infiltration. Prior to that time, the rate of infiltration is not expected to equal outflow from the drum. Data shows that infiltration remained relatively steady (~0.26 l/s) from t = 10 minutes until fluid addition was stopped ~36 minutes after starting the test, for a total volume of ~640 liters; an appendix to the CD-ROM version of this document contains the data.

return

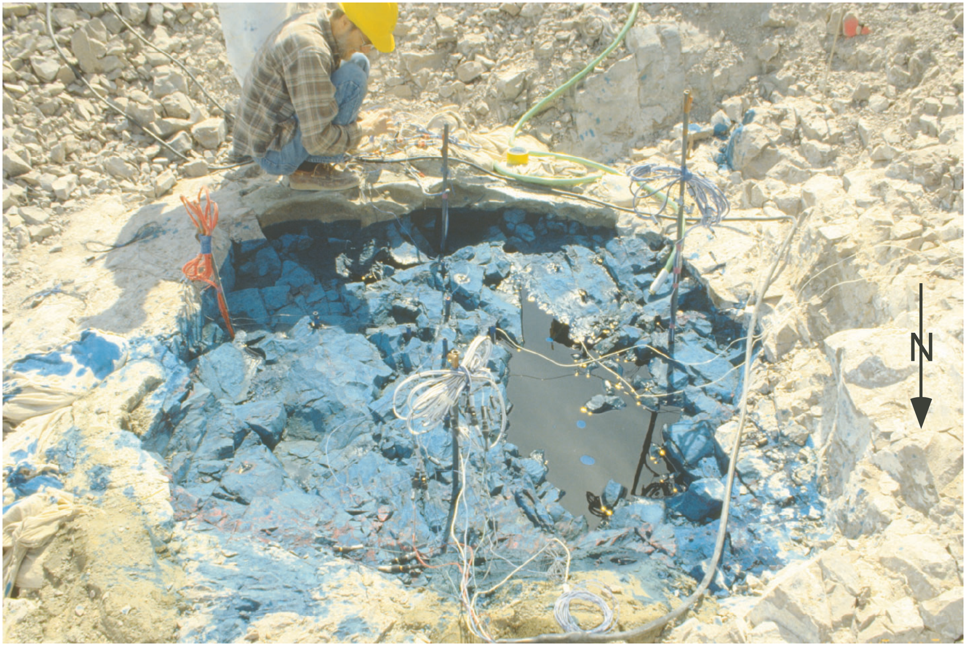

Figure 3.6 - conclusion of infiltration: Fluid supply to the pond was halted 36 minutes after initiating flow. Remaining fluid in the pond quickly drained into the fracture network, leaving only a small amount of fluid trapped at the surface, as seen in this view looking to the south. Extremely low permeability of the rock matrix prohibited significant imbibition. The trapped fluid was lost through evaporation and slow flow through small fractures. Fresh surfaces chipped into the heavily stained floor of the pond showed no evidence of imbibition into the rock matrix. In addition to the ~150 liters added to start the test (see figure 3.3 - initiation of flow), ~640 liters of fluid were added from the supply drum during the 36 minutes of metered flow (see figure 3.4 - infiltration) for a total infiltration volume of ~790 liters.

Nicholl and Glass, 2002

return

Figure 3.7 - tracer stain after 24 hours: The tracer for this experiment (4 g/l of FD&C Blue #1 food coloring) was chosen for negligible environmental impact, strong sorption onto the fracture surfaces, and high visibility. In this view from north of east, taken twenty-four hours after infiltration, ultraviolet radiation has partially degraded the visible tracer (see figure 3.6 - conclusion of infiltration); however, the rate of degradation declines rapidly with time, and tracer exposed to sunlight remained visible for days to weeks. Tracer protected from sunlight (i.e., in the unexcavated fracture network) did not degrade appreciably, nor did it remobilize. As compared to the unstained rock, the tracer clearly accentuates the fracture network (see figure 3.2 - infiltration pond prior to test). The four main ERT strings (taller PVC pipes, one is marked by the white arrow) formed a 1.5 x 1.5 m square within the infiltration pond (see figure 3.8 - ERT array).

Nicholl and Glass, 2002

return

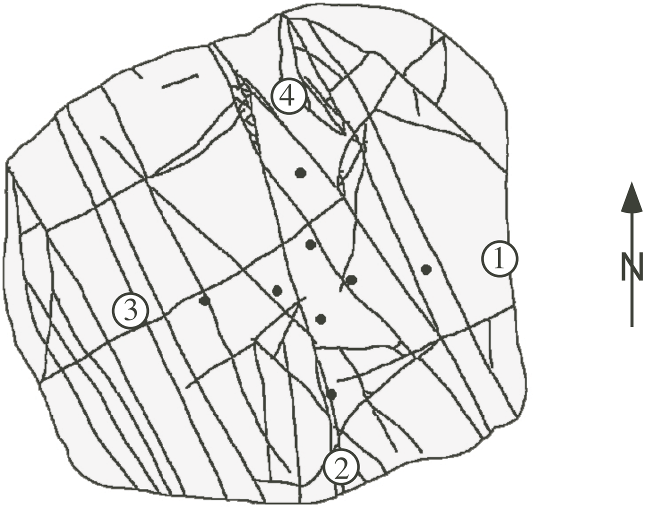

Figure 3.8 - ERT array: Infiltration pond and ERT array. The gray region outlined in black represents the area excavated for the pond, black lines within the pond represent fractures. Investigators from LLNL (B. Daily and A. Ramirez) explored the utility of Electrical Resistance Tomography (ERT) for detecting water content changes in a fracture network by measuring resistivity over a set of two-dimensional vertical planes beneath the infiltration pond before, during, and after infiltration. Four ERT strings, each 3 m long and containing 11 electrodes (30 cm apart) were grouted into dry drilled vertical holes located within the pond at the corners of a 1.5 x 1.5 m square (numbered circles). Eight shallow (~15 cm) surface electrodes (solid circles) were installed along diagonals of the square (see figure 3.2 - infiltration pond prior to test) to increase resolution in those planes. Because the infiltration rate was unexpectedly high, measurements during infiltration were limited to two sequential cross-hole ERT resistance fields in the plane between strings 1 and 3. The full suite of measurements (i.e., resistivity fields between all string pairs) were measured on the day before the test, over the hour following infiltration, and on the next day.

Nicholl and Glass, 2002

return

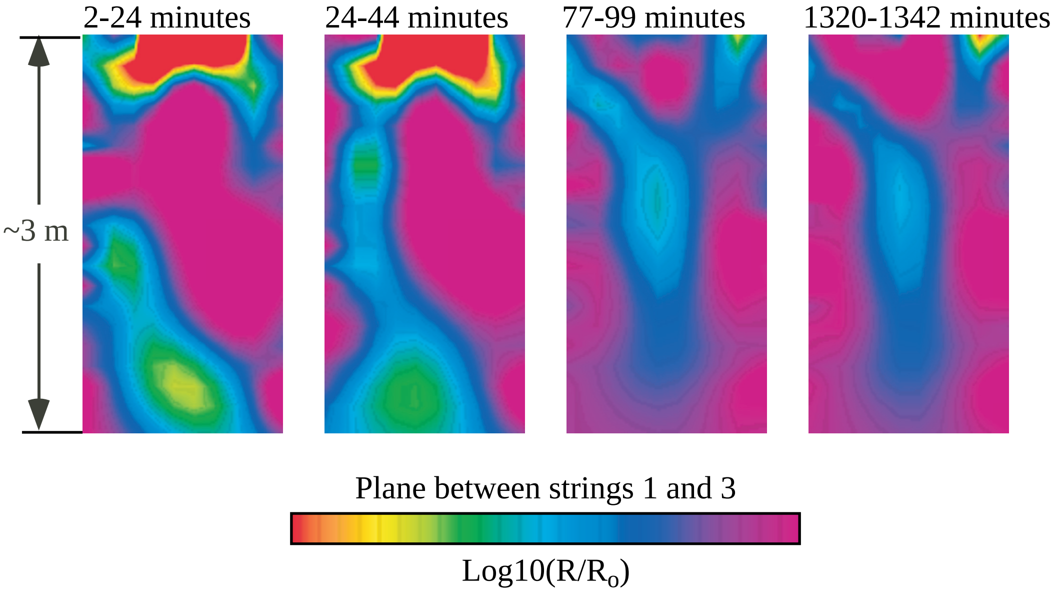

Figure 3.9 - ERT results: ERT data was only reduced in a preliminary fashion, as can be found in the archived scientific notebooks [LLNL YMP controlled scientific notebook LBT-03, 3/4/94, pp. 5-26]. The images shown above represent a 1.5 m wide by 3.0 m deep plane between electrode strings 1 and 3 (figure 3.8 - ERT array) and are calculated with data collected over a 22 minute period. Each image depicts the log change in resistivity with respect to baseline data collected before infiltration (i.e., Log10 R/Ro). Over the period from 2-24 minutes after initiating infiltration, sharp decreases in resistivity are seen to extend from the surface pond through the base of the 3 m imaging depth; localization of decreased resistivity in the ERT image suggests significant preferential flow within the pervasive fracture network. Note that in both images taken during infiltration (2-24 and 24-44), the surface pond exerts a strong influence on measured resistivity (i.e., bright red zone at the top of both images). After ending infiltration (36 minutes) resistivity quickly returns to near initial conditions, suggesting rapid drainage. Additional images and interpretation may be found in Glass et al. [2002].

Nicholl and Glass, 2002

Section 4 - Excavation and Mapping

Infiltration was performed on 3/11/94, excavation for the LLNL Large Block resumed approximately 8 weeks later (5/3/94). At that time, we began to collect data on the fracture network and distribution of tracer at locations directly below our three infiltration sites. We continued to collect data throughout the course of excavating material from around the LLNL Large Block. This set of images shows s activities occurring during the excavation process (5/3/94 to 8/2/94). We have included images illustrating our mapping activities, and the excavation process itself. We have also included a series of shots showing removal of the cap from the LLNL Large Block.

return

Figure 4.1 - start of excavation: View looking eastward and down onto the work site following the first round of excavation. Articulated arm of the tracked vehicle (hoe ram) carries an impact hammer with a 0.5 m long chisel. The hoe ram was used to shatter the rock pavement surrounding the LLNL large block, which is seen at the center of the image. After breaking up the pavement to a depth of ~0.5 m, rubble was removed with a small bulldozer (see figure 4.5 - mapping the large block). In order to maintain integrity of the Large Block during excavation, it was capped in concrete and placed under compression using rock bolts extending from bedrock to the steel cross on top of the concrete cap (3 x 3 m in plan). Blue stained rubble from our ponded infiltration experiment can be seen in the lower right hand corner of the image.

return

Figure 4.2 - wire saw in action: At an intermediate stage of the excavation, the concrete cap topping the LLNL Large Block was cut off with a wire saw. Fixtures attached to the Large Block guided a continuous loop of diamond studded steel cable as it was circulated around, and drawn through the block. In this view, looking to the northeast, the drive mechanism and controls for the wire saw are seen on the right hand side of the image; a wooden wall was erected to protect the operator in the event of cable breakage. Hoses inserted into the saw cut (red arrow) added small amounts of cutting fluid (water). Cutting operations were completed within a 48 hour period. At the time of this activity (5/17 to 5/19/94), the portable wire saw had recently been used to cut apart freeway overpasses following the Northridge (Southern California) earthquake.

return

Figure 4.3 - removal of the concrete cap: On 5/19/94, the concrete cap on top of the LLNL block was removed. This was a critical operation in the LLNL excavation process, as failure of the cap during removal could have damaged the Large Block. In order to provide access for the crane and flat bed truck a temporary ramp had to be erected (see figure 2.8 - bench face). Wooden wedges and slats seen on top of the Large Block (lower land hand side of image) were inserted into the saw slot to support the cap during cutting. Rubble in the foreground is typical of that produced by the hoe ram. This view from above our ponded infiltration test, looks slightly north of east, towards Forty Mile Wash and the Calico Hills (see figure 2.3 – Yucca Mountain satellite image).

return

Figure 4.4 - sawn surface: Looking from the west onto the top of the LLNL Large Block after lifting off the concrete cap (see figure 4.3 - removal of the concrete cap). Dark regions are damp following removal of cutting debris. The curvilinear nature of the dark regions reflects cutting action of the wire saw (see figure 4.2 - wire saw in action). Smooth horizontal surfaces such as the 3 x 3 m top of the Large Block are excellent for mapping fracture trends and connectivity (see figure 4.6 – fracture connectivity); but do not allow for measurement of inclination in tight fractures. Our pavement surfaces were extremely rough (see figure 4.10 - mapping) which made it difficult to trace individual fractures; however, exposed fracture surfaces allowed measurement of inclination on most fractures.

return

Figure 4.5 - mapping the Large Block: After the concrete cap was removed from the Large Block (see figure 4.3 - removal of the concrete cap) investigators from LLNL mapped fractures intersecting the top of the block (see figure 4.6 - fracture connectivity). The yellow bands are part of a clamping system designed to maintain integrity of the Large Block during subsequent excavation. The Large Block was also protected by a buffer zone that extended approximately 1 m in all directions; the buffer zone was sampled and removed (see figure 4.7 - excavation in process) in the final stage of excavation. The bulldozer was used to remove rubble from the excavation, and push it down slope to the east. In this view to the northeast, Forty Mile Wash and the Calico Hills are seen in the background (see figure 2.3 – Yucca Mountain satellite image).

Nicholl and Glass, 2002

return

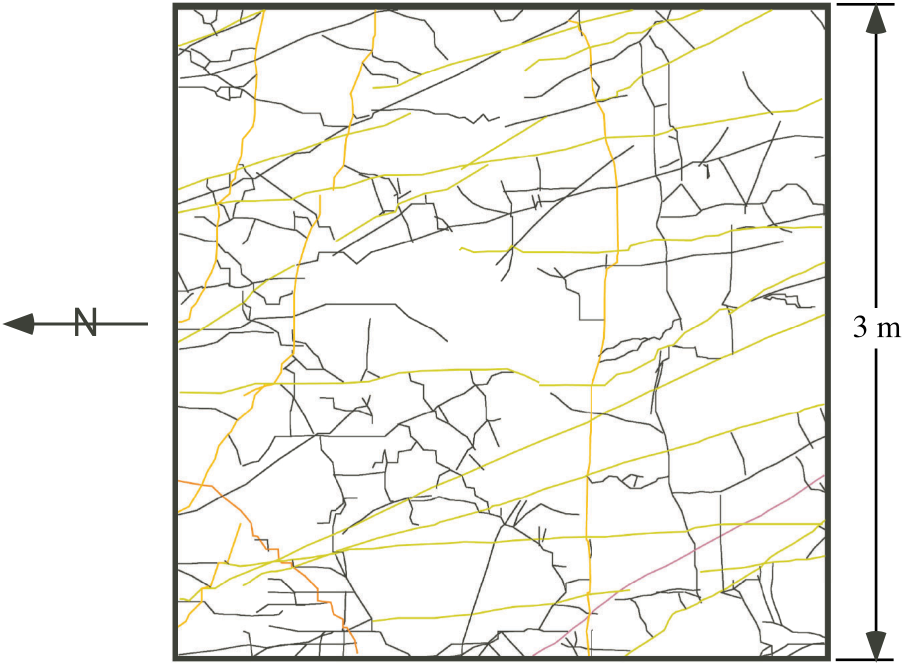

Figure 4.6 - fracture connectivity: This map of fracture traces intersecting the top of the LLNL Large Block (see figure 4.5 - mapping the Large Block) was modified from Wagoner [1999]; colored lines represent fractures that were assigned to specific joint sets. Orientation of this view (east at the top) was chosen to facilitate comparison with the photograph of this surface that is shown in figure 4.4 - sawn surface. Several fractures are of sufficient size to span the system, and a large number of cross-cutting relations are evident. The strong connectivity observed here is consistent with pavement maps beneath our ponded infiltration test (located 3-4 m southwest). In addition to the top, investigators from LLNL also mapped fracture traces on the vertical sides of the Large Block [Wilder, et al., 1997; Wagoner, 1999]. Wagoner [1999] produced a 3-D model of the primary fracture sets within the LLNL Large Block, incorporating data from both the surface maps and video logs of numerous boreholes within the Large Block.

Nicholl and Glass, 2002

return

Figure 4.7 - excavation in process: This view of the excavation, taken from slightly south of east, shows removal of the buffer zone (figure 4.5 - mapping the Large Block) surrounding the LLNL Large Block. Articulated arm of the hoe ram was used to carefully remove material immediately adjacent to the Large Block. Large samples were taken from the vertical slab jutting outwards from the Large Block; sides of the slab were cut with the belt saw (see figure 2.7 - belt saw). Black plastic on top of the Large Block was later replaced with white plastic to minimize heat build-up and subsequent moisture redistribution. Dust cloud on the left hand side of the image results from cleaning the pavement beneath our ponded infiltration test prior to mapping. Operator of the air pipe can barely be seen within the dust cloud (see figure 4.9 - cleaning the pavement).

return

Figure 4.8 - end of excavation: The hoe ram (see figure 4.1 - start of excavation) is nearly hidden behind the LLNL Large Block (3 x 3 x 4.5 m) in this view from the east. Here, near the end of excavation, the hoe ram is working ~5 m directly below the site of our ponded infiltration test (see also figure 2.8 - bench face). The LLNL Large Block is covered in translucent plastic for protection (see also figure 2.4 - site on Fran Ridge). As the ~1 m buffer zone surrounding the Large Block was stripped away, additional compression bands (yellow) were added to help maintain structural integrity (see also figure 4.5 - mapping the Large Block). Chain link fencing was installed on the excavation walls to mitigate rock fall events.

return

Figure 4.9 - cleaning the pavement: At each excavation level, the hoe ram pulverized the rock surface, producing rubble that varied in size from rock flour to boulders. Larger rubble was removed with a bulldozer (see figure 4.5 - mapping the Large Block); however, our mapping activities required the pavement be cleaned to bare rock. Fine rubble was removed by hand; first with a shovel, and then an air pipe. Due to the time and expense involved with this detailed cleaning, only the areas to be mapped were cleared. At each of our infiltration sites (see figure 2.5 – site map), vertical holes were dry drilled at opposing corners of the mapped area following infiltration. Paint marks on the excavation walls provided a rough guide to the location of these holes. Once the vertical holes were found, just enough pavement was cleaned to set out the mapping grid (see figure 4.10 - mapping).

return

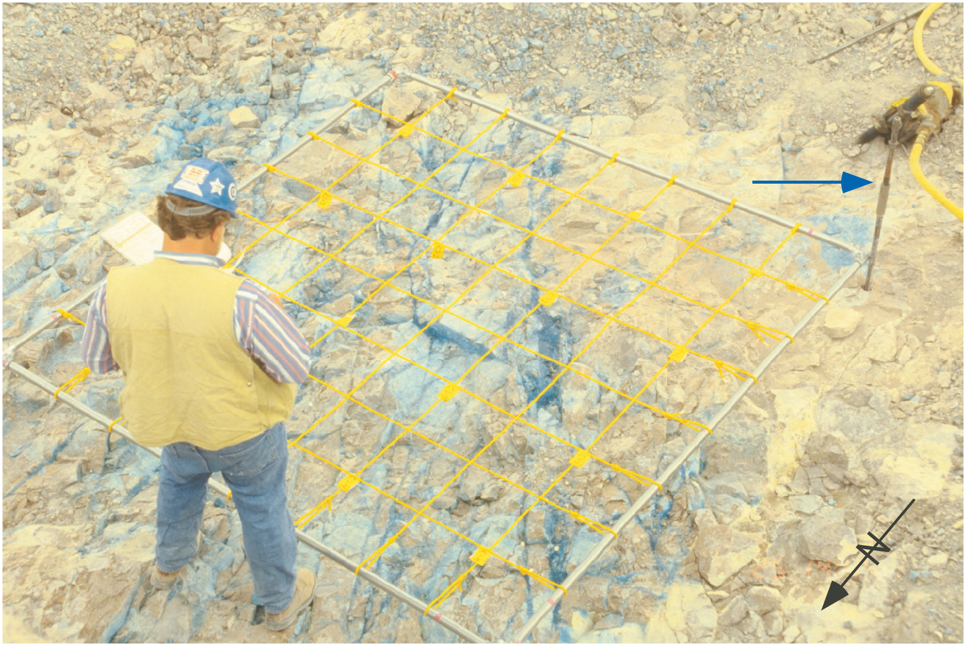

Figure 4.10 - mapping: At each excavation level, the distribution of tracer and fractures were mapped directly beneath the infiltration site at a scale of 1:12. Maps were referenced to a portable 2.44 x 2.44 m (8 x 8') grid subdivided at 0.305 x 0.305 m (1 x 1') intervals. Here, in this view looking to the southeast, D. Engstrom (SNL) is mapping beneath the site of our restricted flow test (site #2 on figure 2.5 - site map); the grid and mapping process was identical at all three infiltration sites. The blue tracer clearly marks both vertical and subhorizontal fractures. In the upper left hand side of the image, tracer clearly extends outside of the area cleaned for mapping and disappears into the rubble covered region. On the right hand side of the image, drill pipe was left standing in one of the vertical locator holes (blue arrow) used to position the grid. Locator holes were dry drilled following infiltration with the air-driven jackleg seen in the upper right-hand corner of the image.

Nicholl and Glass, 2002

return

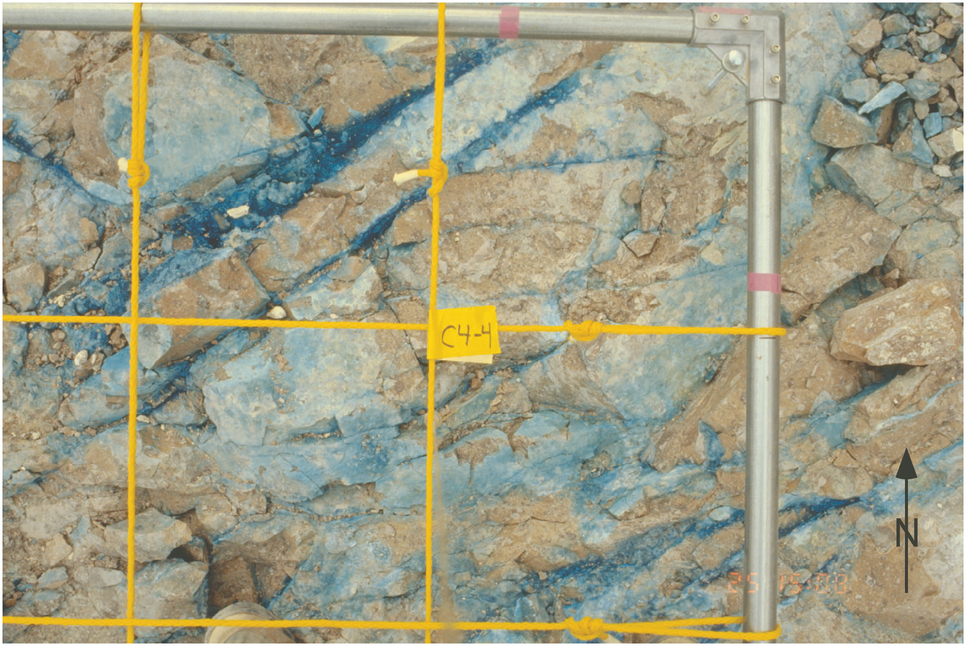

Figure 4.11 - close-up of pavement surface: Each pavement map is a hand-drawn sketch of the distribution of tracer and fractures within the mapped area. Fractures were mapped in order of decreasing size; extensive fractures were mapped first and then smaller features as time allowed. Surface roughness resulting from the excavation method greatly complicated mapping activities by making it difficult to see true fracture connection. This example shows the northwest corner of the 2.44 x 2.44 m (8 x 8’) mapped area ~0.5 m beneath the restricted flow test (site #2 on figure 2.5 - site map); the yellow rope defines grid blocks 0.305 x 0.305 m (1 x 1’) in size. Here, near the infiltration surface, vertical fractures are thoroughly stained with the tracer. Although the excavation method commonly damaged the surfaces of subhorizontal fractures, the remaining fragments seen here are also stained.

Nicholl and Glass, 2002

Section 5 - Mapping Results (ponded test)

During the LLNL excavation process, we mapped the fracture network and tracer distribution over a series of horizontal pavements located directly beneath our ponded infiltration site. Data was obtained over a ~6 m^2 area (8’ x 8’) at roughly 0.5 m vertical intervals. Pavements were mapped at the infiltration surface (level 0), and 11 subsequent excavation levels (levels 1-11) over a depth of ~5 m. We also observed occurrence of tracer outside of the mapped region during excavation of the surrounding rock. Those two data sets were combined to estimate the extent of the flow field resulting from the infiltration test. We also extracted data on fracture trace length and orientation from pavement maps collected beneath the ponded infiltration test. A simple modeling study based on this data has been reported by Eaton et al. [1996a,b] where both dual-permeability and equivalent-continuum approaches were applied. As one might expect, the two approaches resulted in strikingly different saturation distributions. And of course, neither displayed the rich variety of behavior observed in the field.

return

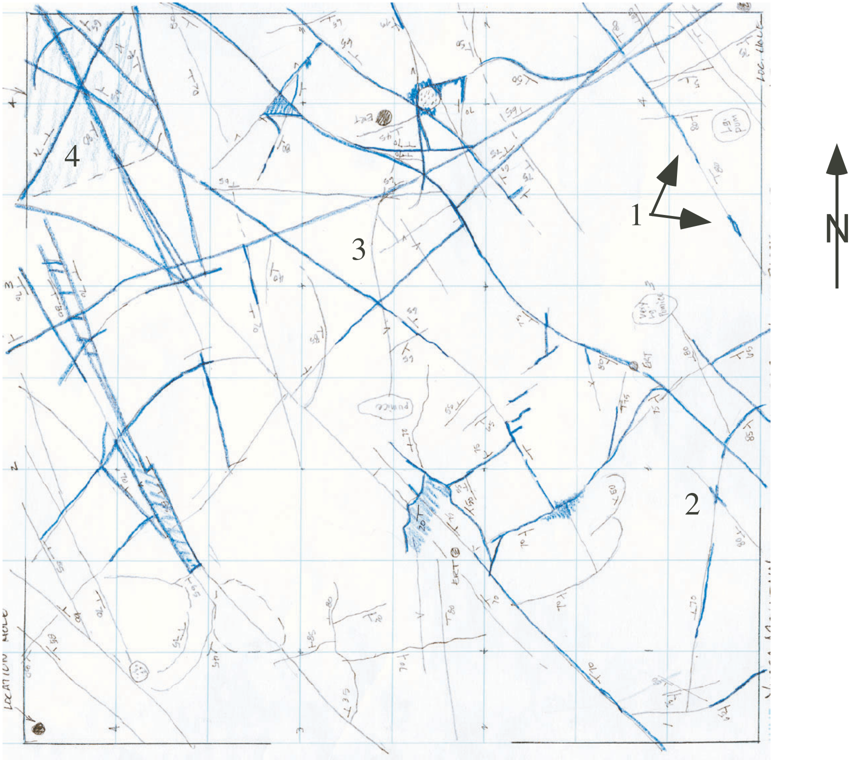

Figure 5.1 - sample pavement map: Example pavement map collected ~3 m below the infiltration surface (level 8). Distribution of tracer is concentrated in the north and northwest portions of the mapped region. The southwest corner of the mapped region was untouched by the flow field at this, and all levels throughout the excavated depth (see figure 5.2 - fracture/tracer maps). The tracer pulse appears to be somewhat split, with the portion to the southeast being fragmented. Within this map, one can see a number of small scale flow features: (1) fragmented flow along a single fracture; (2) concentration of flow at fracture intersections; (3) bypassing of fractures, despite obvious physical connection to the flow field; and (4) flow on subhorizontal features. An appendix to the CD-ROM version of this document contains digital copies of the pavement maps.

Nicholl and Glass, 2002

return

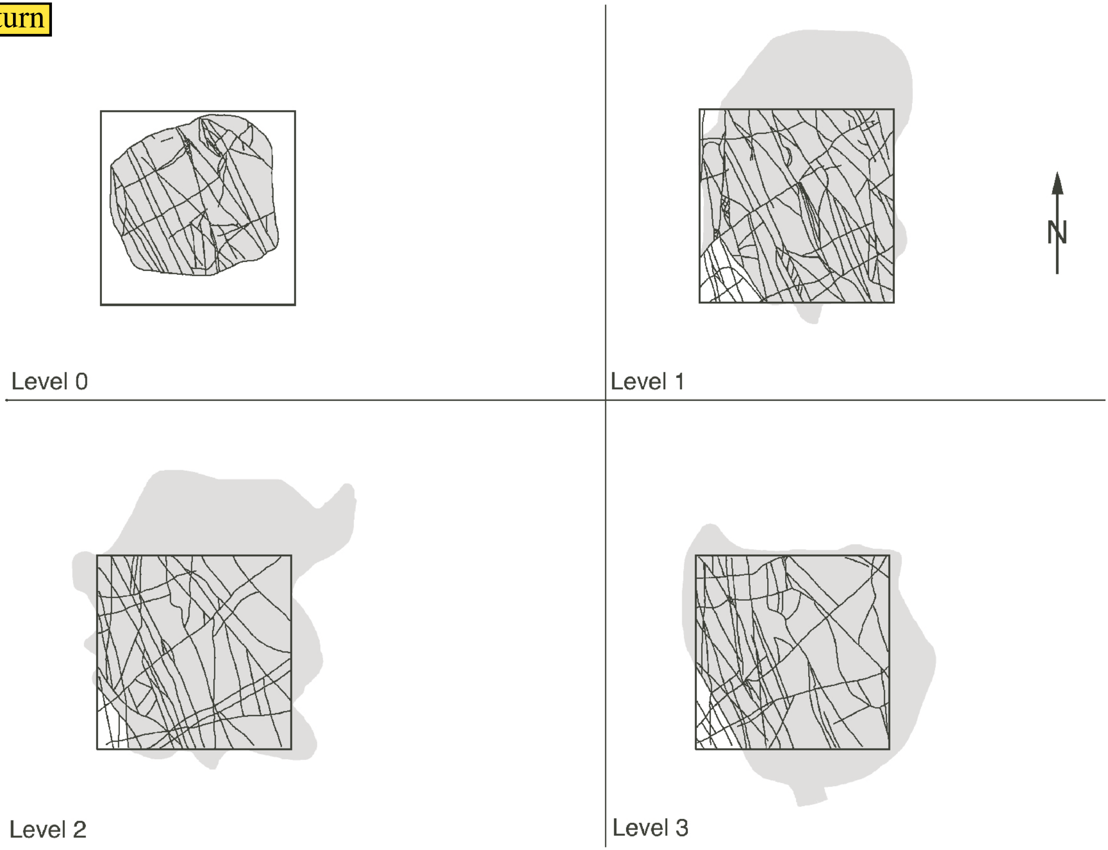

Figure 5.2 - fracture/tracer maps: This, and the next two pages contain fracture pavement maps for levels 0 through 11; areas in which tracer was observed are shown in gray. Level 0 is the infiltration surface, where mapping was limited to areas within the infiltration pond. At each level, the mapped region is outlined; estimates of tracer location outside that region are based on 35 mm slides and notes taken during the excavation process. Details of how these maps were developed can be found in Glass et al. [2002]; full resolution copies of these images can be found in an appendix to the CD-ROM version of this document.

return

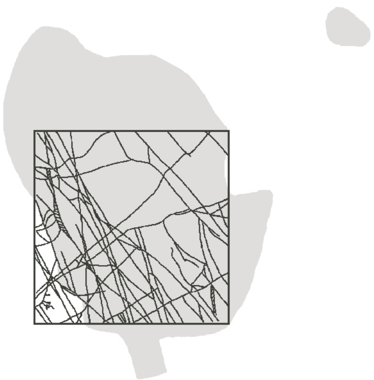

Level 4

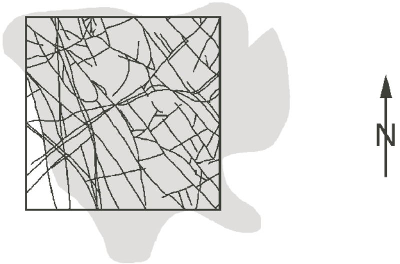

Level 5

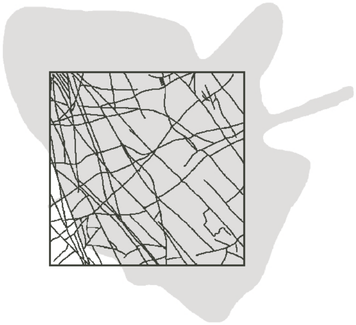

Level 6

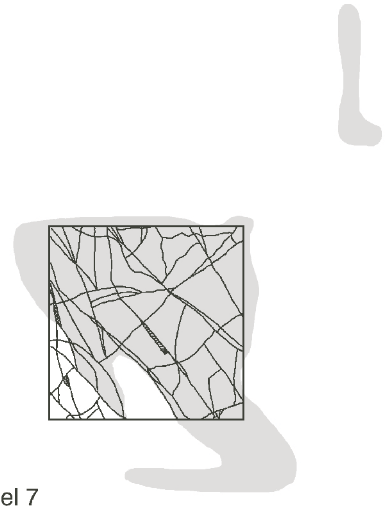

Level 7

Nicholl and Glass, 2002

return

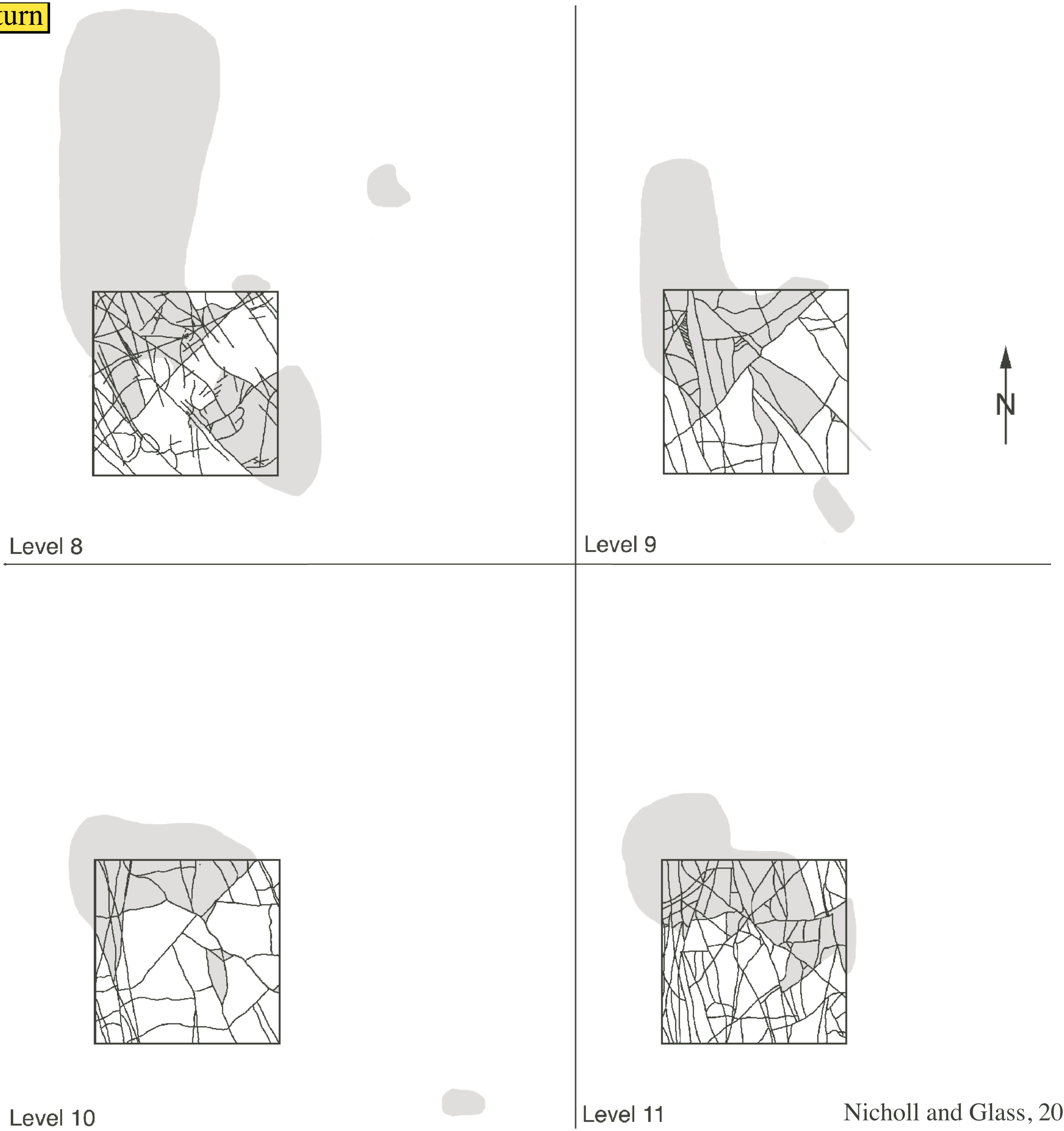

Nicholl and Glass, 2002

return

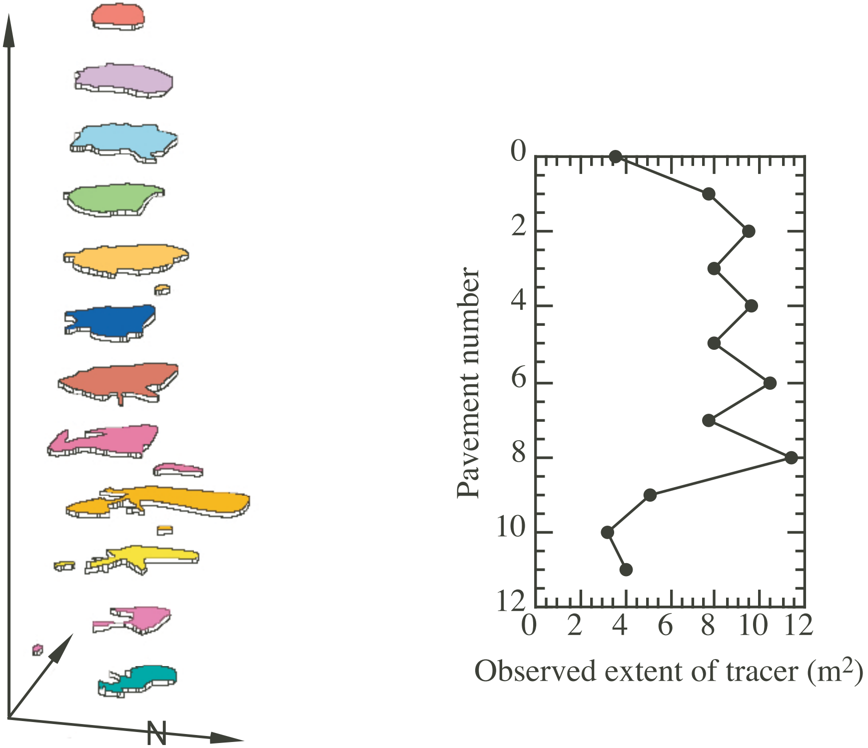

Figure 5.3 - estimated tracer extent: Three-dimensional perspective of the tracer extent (i.e., gray regions in figure 5.2 - fracture/tracer maps) illustrates lateral variability in the flow field with depth. This diagram has been expanded in the vertical direction to enhance discrimination between the various mapping levels. The plot shows the estimated lateral extent of tracer at each level of the excavation; on average, pavements were separated vertically by ~0.5 m. Estimated extent of the flow field is seen to increase rapidly directly below the infiltration pond, oscillate near the larger value, and then contract significantly near the bottom of the excavation.

Nicholl and Glass, 2002

return

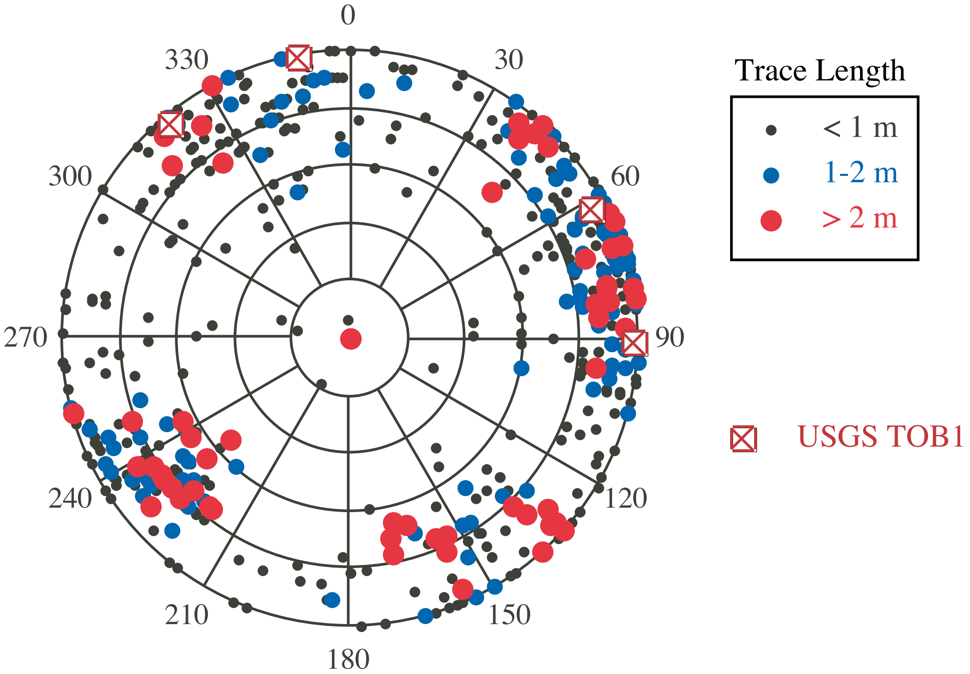

Figure 5.4 - fracture orientations: Dip was measured for ~77% of the mapped fractures; this data set can be found in an appendix to the CD-ROM version of this document. We were unable to measure fractures that did not have an exposed surface, which was most likely to occur for small aperture, near vertical fractures. Poles of the measured planes are plotted on a polar equal-area projection. Data is subdivided into three groups on the basis of measured trace length (0-1 m, 1-2 m, and >2 m). Data shows at least two groups of steeply dipping, extensive (trace length > 2 m) fractures. Measured orientation of the smaller fractures shows more scatter than that for the extensive features. Our measurements are consistent with median orientations of four joint sets measured at an adjacent site by the USGS [Throckmorton et al., 1995]. The USGS site (identified by Throckmorton et al. as TOB1) consisted of a pit and pavement located immediately south and west of our experiment (see figures 2.4 - site on Fran Ridge, and 2.5 – site map).

Nicholl and Glass, 2002

return

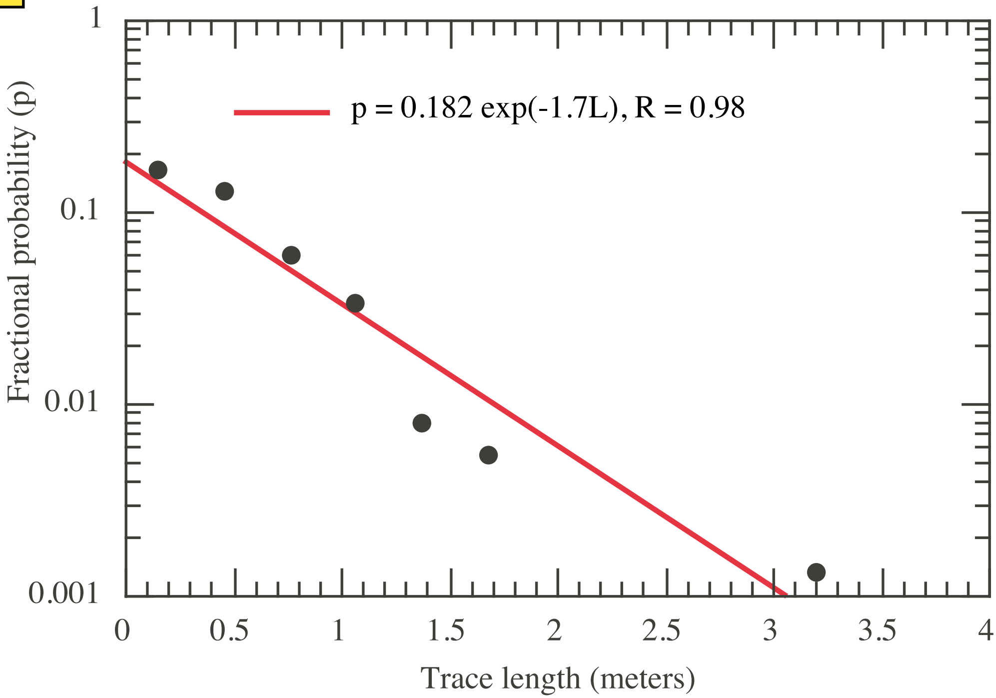

Figure 5.5 - fracture trace length: A mechanical map measure was used to estimate trace length of each mapped fracture, no corrections were made for either dip or apparent variability induced by the rough pavement surface. Trace length data is included in an appendix to the CD-ROM version of this document. Fracture trace lengths commonly display an exponential distribution, with the probability of occurrence (p) for a specific trace length (L) given by $p \propto \exp(CL)$ [Call et al., 1976]. Approximately 60% of the measured fractures at this site extended past the boundaries of the mapped area. The remaining 40% exhibited an exponential distribution, with $C = \sim 1.7$. We also note that Throckmorton et al. [1995] reported extensive fractures (up to 10 m) nearby.

Nicholl and Glass, 2002

Section 6 - Images Denoting Maximum Tracer Extent (ponded test)

Images in this section illustrate lateral migration of the tracer from the ponded infiltration test.

return

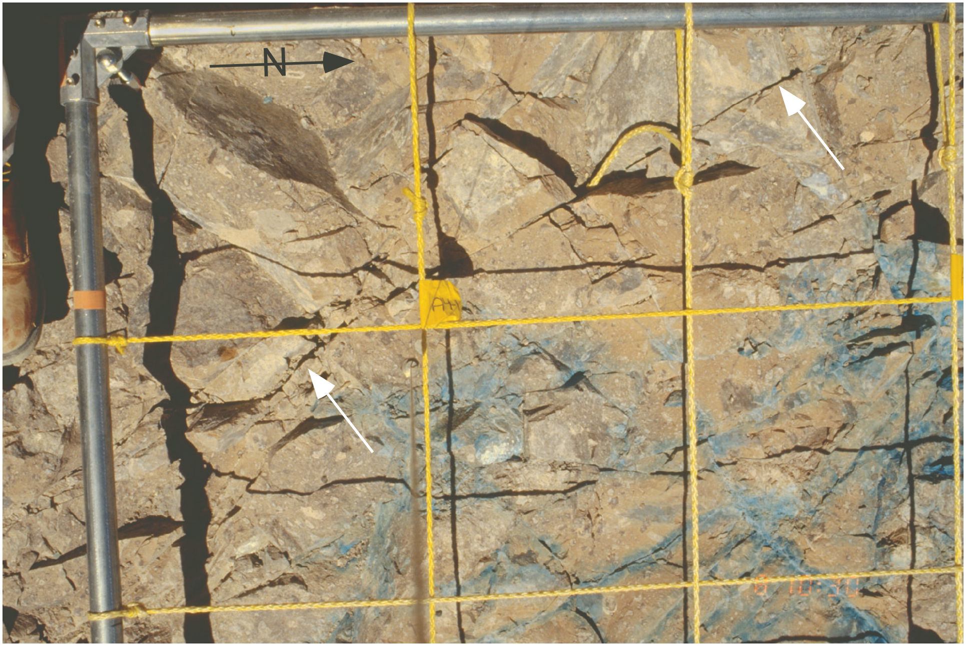

Figure 6.1 - capillary barrier: Southwest corner of the mapped region at a depth of ~2.5 m below the infiltration surface (level 6); yellow grid ropes are separated by 0.305 m (1’) in each direction. Tracer is clearly evident on pavement in the northeast portion of this image, but not to the southwest of a near-vertical fracture (marked with white arrows). The flow field was not observed to enter this corner of the mapped region throughout the excavated depth (see figure 5.2 - fracture/tracer maps), suggesting that this persistent near-vertical fracture may have bounded the flow field by acting as a vertical capillary barrier.

return

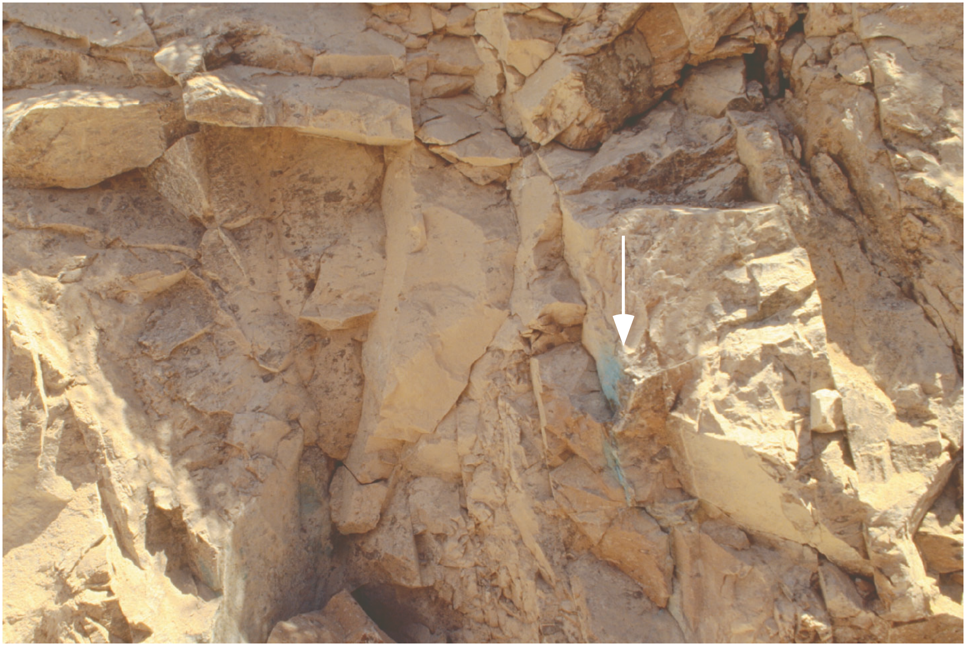

Figure 6.2 - invasion of the south wall: Isolated tracer on an extensive near-vertical fracture exposed in the excavation wall ~1 m south of the mapped region, and ~1 m beneath the infiltration surface (see figure 5.2 - fracture/tracer maps). The exposure shown in this image covers ~1 - 1.5 m^2. Despite the densely fractured network, tracer was only found on the single vertical fracture (white arrow), which extended into the mapped region beneath our infiltration site. Also, tracer only partially covered the fracture plane.

return

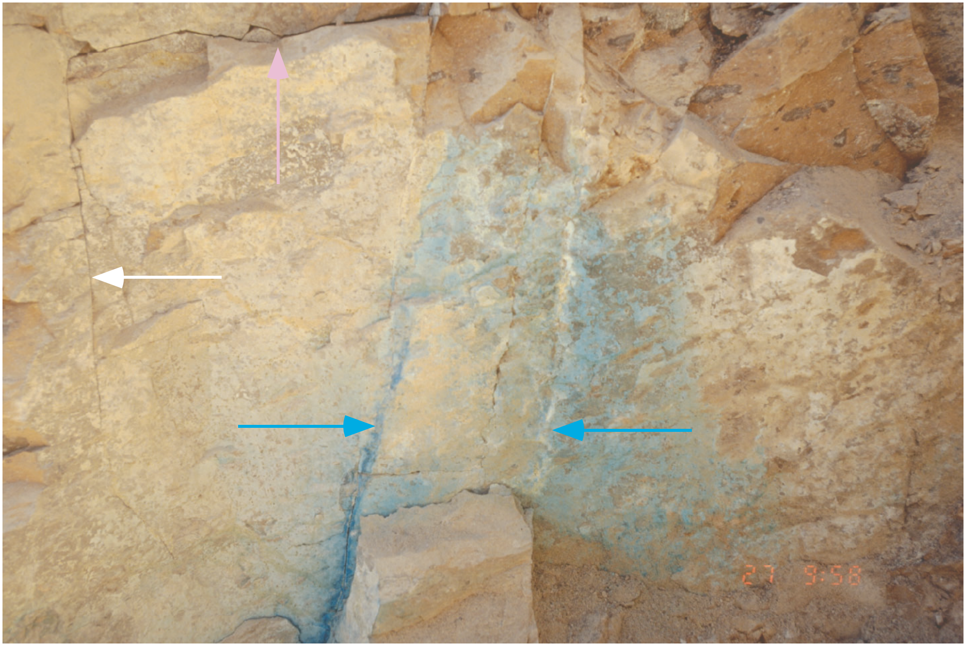

Figure 6.3 - localized tracer on the south wall: Tracer on the surface of an extensive near-vertical fracture exposed in the excavation wall ~1 m south of the mapped region and ~1 - 1.5 m below the infiltration surface. The exposure shown in this image covers ~0.5 m^2. The flow field contacted a limited portion of this surface, which belongs to a fracture that did not pass through the mapped region directly beneath the infiltration pond. Connection to the infiltration surface appears to have occurred through the two near-vertical fractures (blue arrows) penetrating into the excavation wall near the center of the photograph (see also figure 5.2 - fracture/tracer maps). Note that a third near vertical fracture near the left edge of the photograph (white arrow), and a sub-horizontal feature (purple arrow) near the top of the image are both devoid of tracer.

Nicholl and Glass, 2002

return

Figure 6.4 - distributed tracer on the south wall: South wall of the excavation ~3 m below the infiltration surface (level 7, see also figure 5.2 - fracture/tracer maps). Tracer is seen to extend over a 1.5 – 2 m long portion of the wall (see white arrows), occupying both vertical and subhorizontal fractures. Chisel and arm of the hoe ram are seen along the right hand edge of the image; the lower of the two purple arrows points to the chisel, and the other to the arm of the hoe ram, which seems to blend into the excavation wall. This image was taken in deep shadow; hence, the green paint on the hoe ram appears similar to the blue tracer (see figure 4.1 - start of excavation).

return

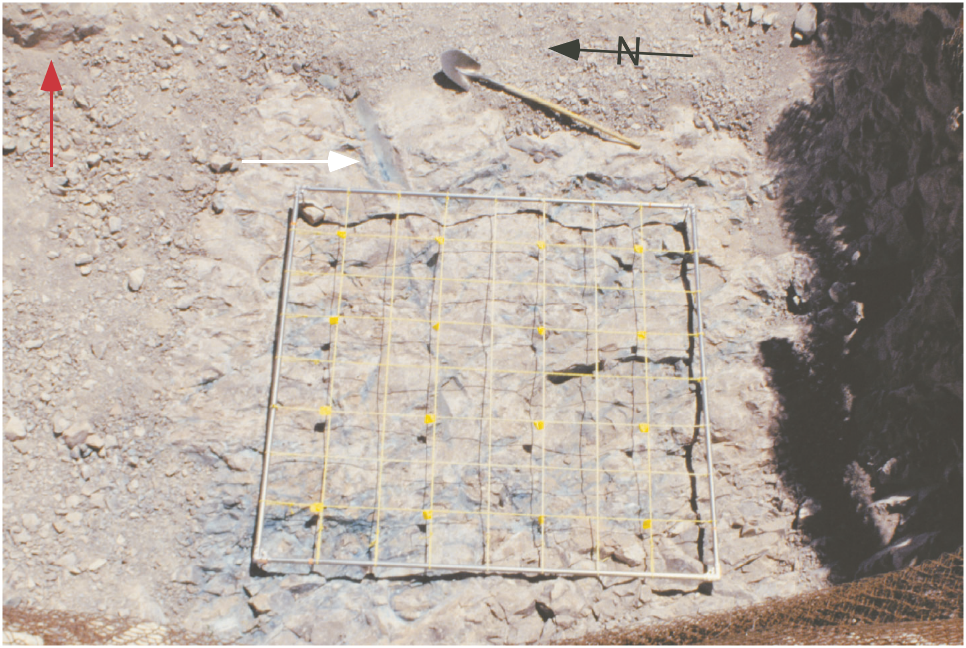

Figure 6.5 - lateral migration in a vertical fracture: View looking down on the 2.44 x 2.44 m (8 x 8') mapped area at a depth of ~2.5 m below the infiltration surface (level 6). Tracer stain is clearly concentrated in the northwest corner of the mapped area (lower left corner of the grid) and extends outward in that direction. A steeply dipping fracture exiting the mapped area in a direction slightly north of east (see white arrow left of the shovel) shows tracer migration away from the mapped area. A close-up view of this fracture is shown in figure 7.5 - upward capillary flow. Buffer zone surrounding the LLNL Large Block (red arrow) can be seen in the extreme upper left hand corner of the photograph (see figure 4.5 - mapping the Large Block).

Nicholl and Glass, 2002

return

Figure 6.6 - tracer in the buffer zone: During excavation, pavements were broken to a distance of about 1 m from the LLNL Large Block. The purpose of this buffer zone (see figure 4.5 -mapping the Large Block) was to minimize the risk of damage to the Large Block and to obtain representative samples at the conclusion of excavation. Here, near the bottom of the image, we see evidence of our tracer on the buffer zone (white arrow) more than 2 m northeast of the infiltration site, at a depth of ~1.5 m below the infiltration surface. This view is from approximately the same location as the red arrow shown in figure 6.5 - lateral migration in a vertical fracture.

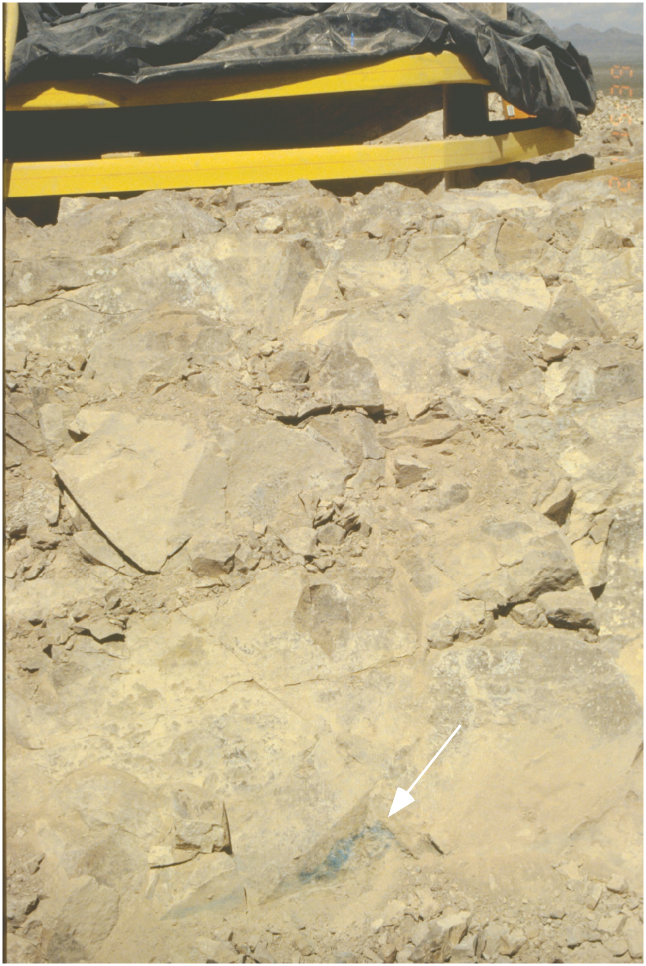

return

Figure 6.7 - excavation bottom: Excavation was halted ~5 m below the infiltration surface (level 11). This image looks towards the southwest from on top of the LLNL Large Block; the 2.44 x 2.44 m (8 x 8’) mapping grid is located directly below our ponded infiltration test. At this depth, the rock mass appeared to be much more competent than at shallower depths, and there was less evidence of subhorizontal fractures exposed in the pavement. While there is some tracer east of the mapped region, the strongest stains are in, and outside of the northwest corner of the grid. Strength of the stain clearly suggests that the infiltration pulse penetrated beneath this level (see also figure 5.2 - fracture/tracer maps).

Section 7 - Local Flow Features

In addition to the large scale mechanisms controlling lateral migration of the tracer, we also observed a number of localized unsaturated flow features. While our principal test (ponded infiltration test) was designed to flood the fracture network near the pond, unsaturated flow occurred further away from the infiltration surface Both of the remaining experiments (restricted flow test and small slug test) were designed to induce unsaturated flow conditions nearer to the infiltration surface.

return

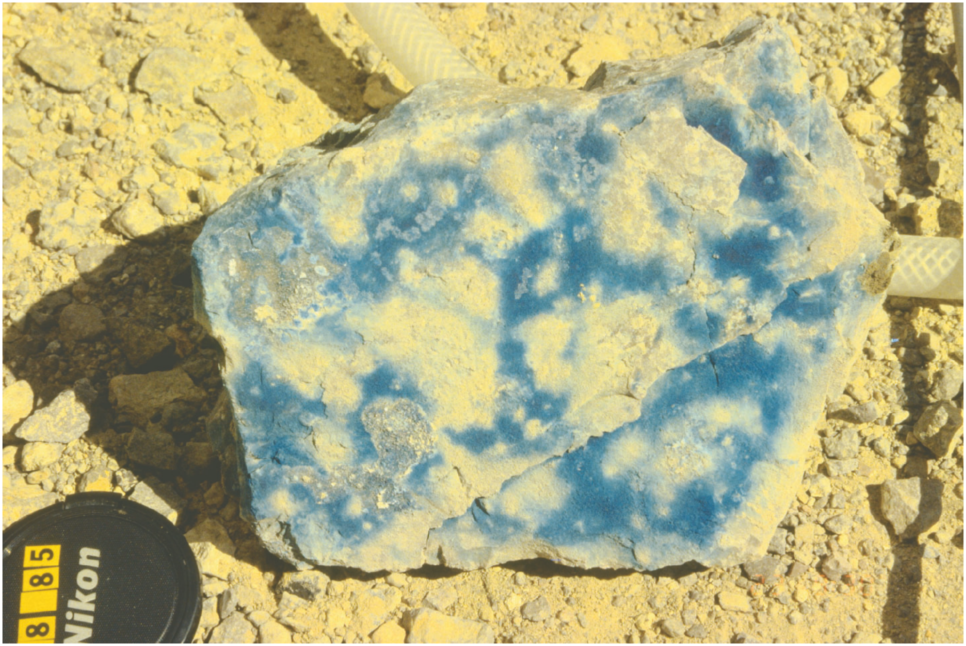

Figure 7.1 - complicated local structure: Tracer staining the plane of a single fracture; lens cap is shown for scale. Sample was found within the excavated rubble near the ponded infiltration test at a depth of ~3-4 m below the infiltration surface; however, the horizontal location is not known. Tracer appears to be connected in all directions, suggesting capillary dominated flow. Large portions of the aperture field were apparently bypassed by the invading fluid. Laboratory and numerical investigations of fluid invasion along the plane of a horizontal fracture [Glass et al., 1997, 1998] have shown that slow displacement of a non-wetting fluid (air) by a wetting fluid (water) can lead to complicated structures such as that seen here. As compared to a fully saturated fracture, this wetted structure would produce a small satiated permeability [Nicholl and Glass, 1994; Nicholl et al., 2000], restrict passage of fluid through adjacent matrix blocks, and afford smaller contact area for imbibition into the adjacent matrix [Glass et al., 1995, 1996].

Nicholl and Glass, 2002

return

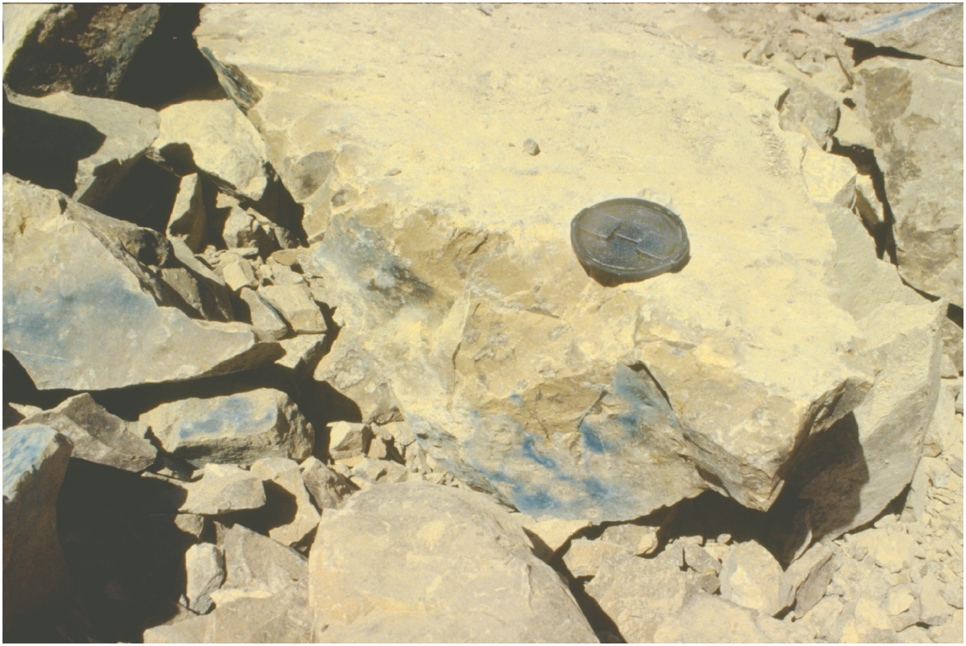

Figure 7.2 – non-uniformity within the flow field: Fracture surfaces excavated at a depth of ~4 m beneath the ponded infiltration test, and 2 – 4 m north of the mapped region show a non-uniform concentration of dye; lens cap is shown for scale. Away from the pond, viscous forces are expected to have been small, and the resultant unsaturated flow would be dominated by competition between capillary and gravity forces. The excavation method did not allow us to determine the in situ orientation of these surfaces; hence the mechanism for preferential flow is unknown. Note that the lens cap is resting on a fracture surface coated by secondary mineralization. Throckmorton et al. [1995] examined fractures at a location several meters to the south and west of our investigation (see figure 2.5 – site map) and reported the presence of both caliche, and non-calcareous secondary minerals (possibly late-stage siliceous deposits).

return

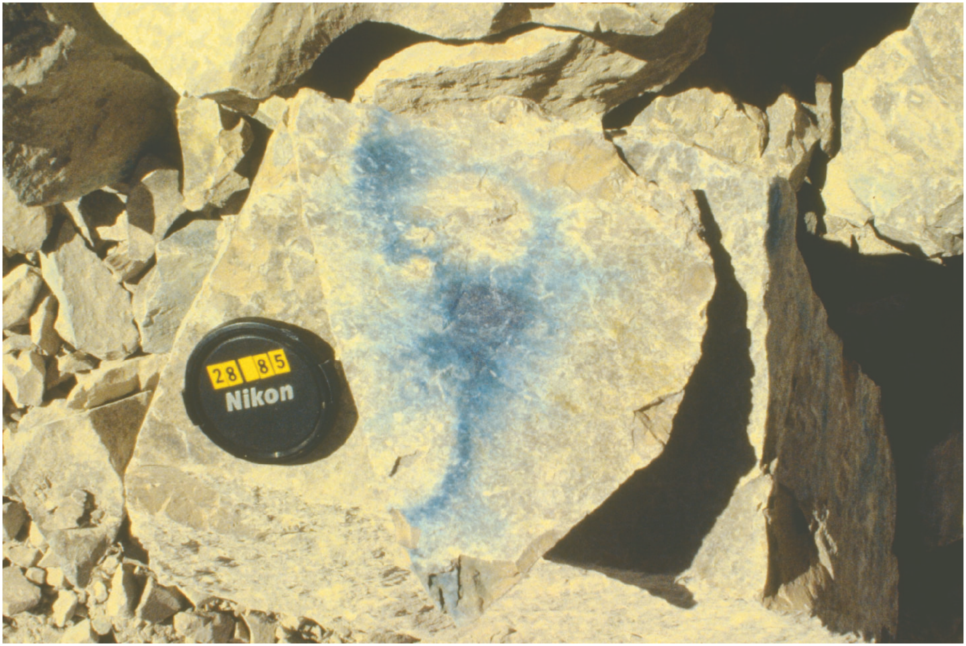

Figure 7.3 - preferential flow: Tracer staining the plane of a single fracture; lens cap is shown for scale. Sample was found within the excavated rubble near the ponded infiltration test at a depth of ~3-4 m below the infiltration surface; however, the horizontal location is not known. Flow structure suggests two pools of fluid within the aperture field. Thin fluid tendrils appear to have connected these pools to each other, and to the main flow structure. While this photo does not provide sufficient data to discriminate between capillary- and gravity-driven mechanisms for preferential flow, flow structure appears remarkably similar to gravity-driven fingers observed during the experiments of Nicholl et al. [1993].

Nicholl and Glass, 2002

return

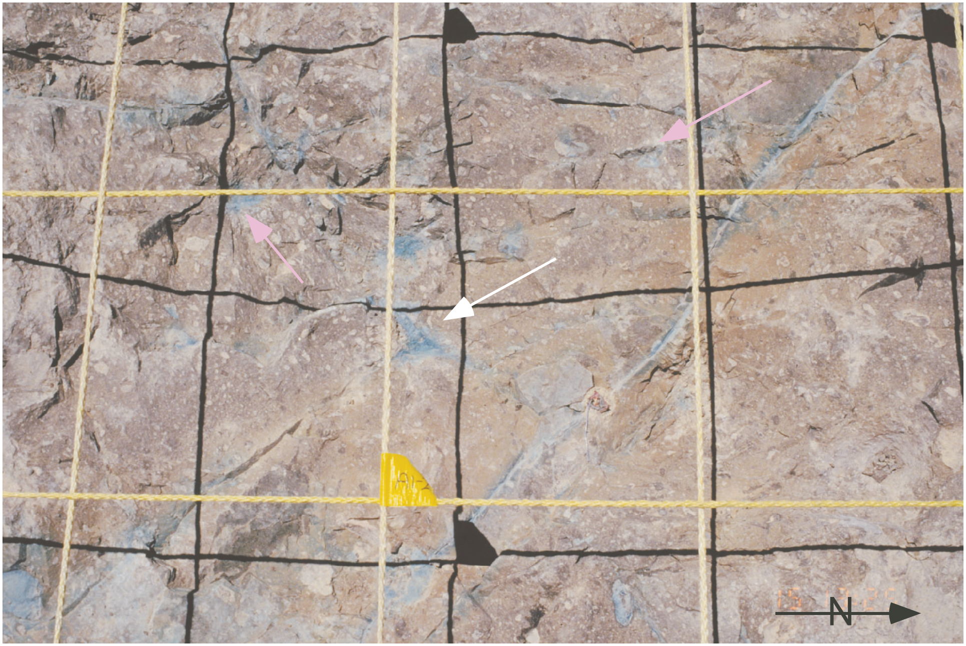

Figure 7.4 - intersections between steeply dipping fractures: A variety of tracer configurations were observed at fracture intersections. This image of the pavement surface was taken at level 7, approximately 3 m directly beneath the ponded infiltration test (see figure 5.2 - fracture/tracer maps); the grid lines are located at 0.305 m (1’) horizontal intervals and ~0.1 – 0.2 m above the rough surface. Here we see an intersection in which one fracture is fully stained (white arrow); however, stain is only observed for a short distance along the other fracture, which trends towards the lower left hand corner of the image. Note that tracer reappears on this fracture near the edge of the image. Above and left of the white arrow, a pumice fragment shows significant absorption of tracer. At other locations (purple arrows), tracer stain marks intersections between hairline fractures that would otherwise be difficult to find.

Nicholl and Glass, 2002

return

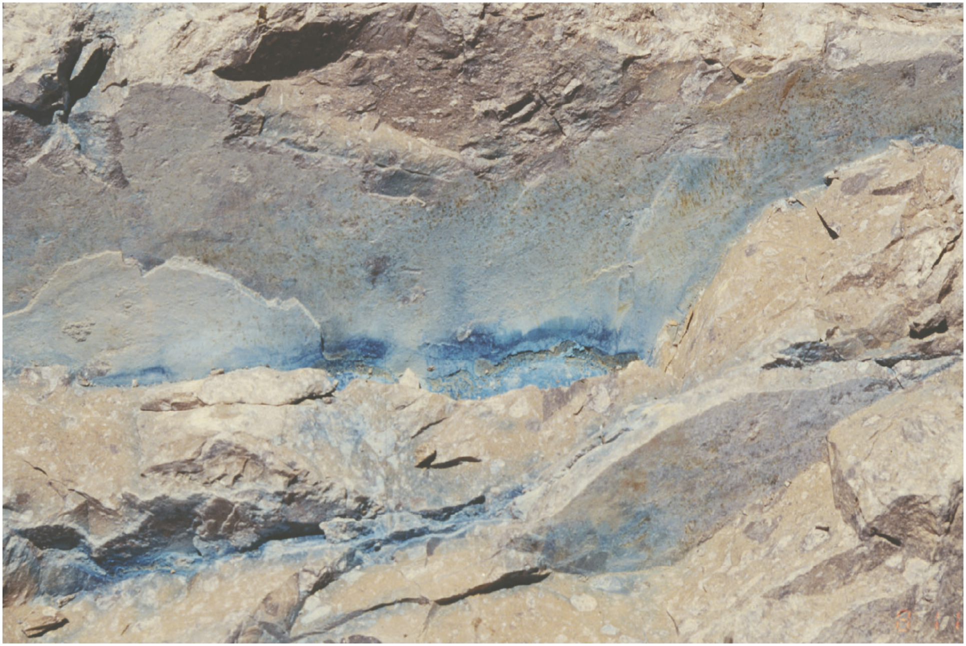

Figure 7.5 - upward capillary flow: Close-up view of a steeply dipping fracture carrying flow away from the mapped area at a depth of ~2.5 m below the infiltration surface (level 6). The view point for this image is the same as that of the white arrow seen in figure 6.5 - lateral migration in a vertical fracture. Dark stain on this steeply dipping fracture fades upwards, suggesting capillary rise. Glass et al. [1995, 1996] suggested that open subhorizontal fractures may act as capillary barriers to downward flow. Fluid may then traverse laterally along the upward edges of such barriers, and be imbibed upwards through capillary action.

Nicholl and Glass, 2002

return

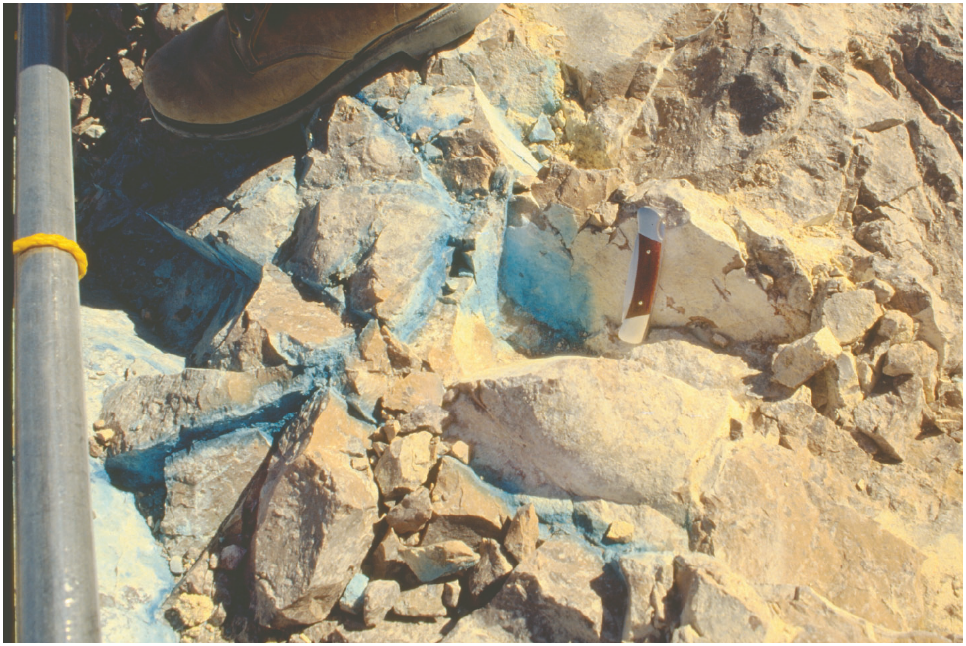

Figure 7.6 - localized flow: This image shows both localized concentration, and absence of tracer along the northern edge of the restricted flow test at a depth of ~1.5 m beneath the infiltration surface. The left hand side of the image is heavily stained, while the right hand side is mostly untouched by the flow field. There are also fractures within the stained region that are free of tracer. Just left of the pocket knife, the flow structure shows a near vertical edge. Continuing leftwards, a star-shaped intersection between three fractures is heavily stained. Extensive fracture coatings at this location appeared to be non-calcareous, and possibly siliceous material emplaced by vapor-phase transport.

Nicholl and Glass, 2002

return

Figure 7.7 - horizontal capillary barrier: Here we see tracer stain on the surface of a near vertical fracture located near the restricted flow test, and about 2 m below the infiltration surface. Stain appears on both sides of the lens cap; but not directly behind it. Left of the lens cap, stain appears both above and below the subhorizontal fracture located at the top of the lens cap. Right of the lens cap, stain is only seen below the subhorizontal fracture. A possible explanation for this structure is that the subhorizontal fracture acted locally as a capillary barrier to upward fluid migration.

Nicholl and Glass, 2002

return

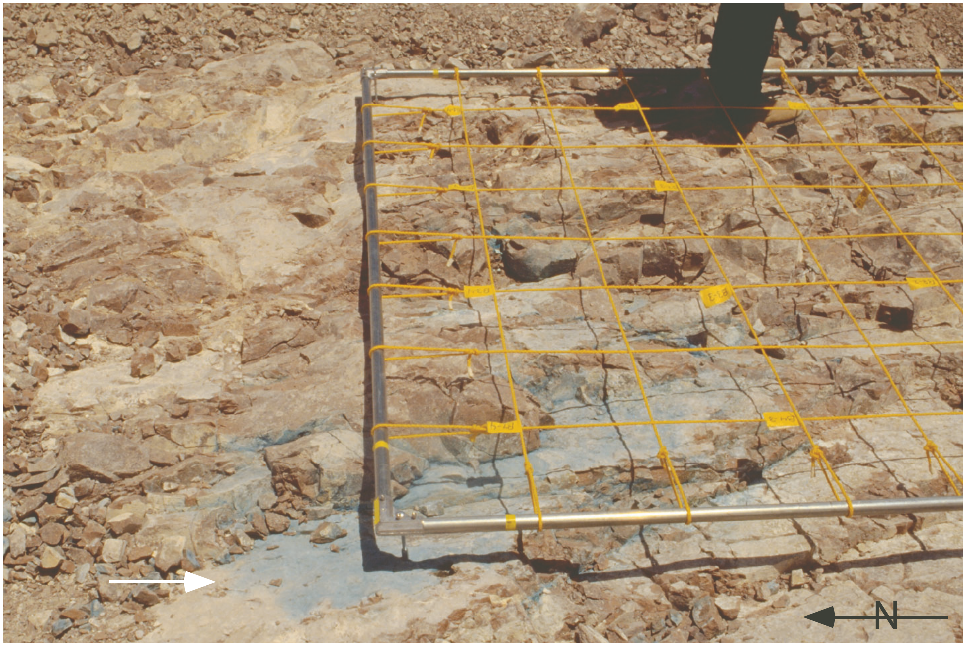

Figure 7.8 - subhorizontal flow: View looking from the west onto the 2.44 x 2.44 m (8 x 8’) mapping grid at a location approximate 0.5 m directly beneath the small-slug test (site 3 on figure 2.5 – site map). Surfaces of stair-step subhorizontal fractures dipping to the northeast show locally pervasive stain, with a clear demarcation between stained and unstained regions (white arrow). Note the extensive secondary mineralization coating the fracture surfaces (see also figures 7.2 – non-uniformity within the flow field, and 7.6 – localized flow).

return

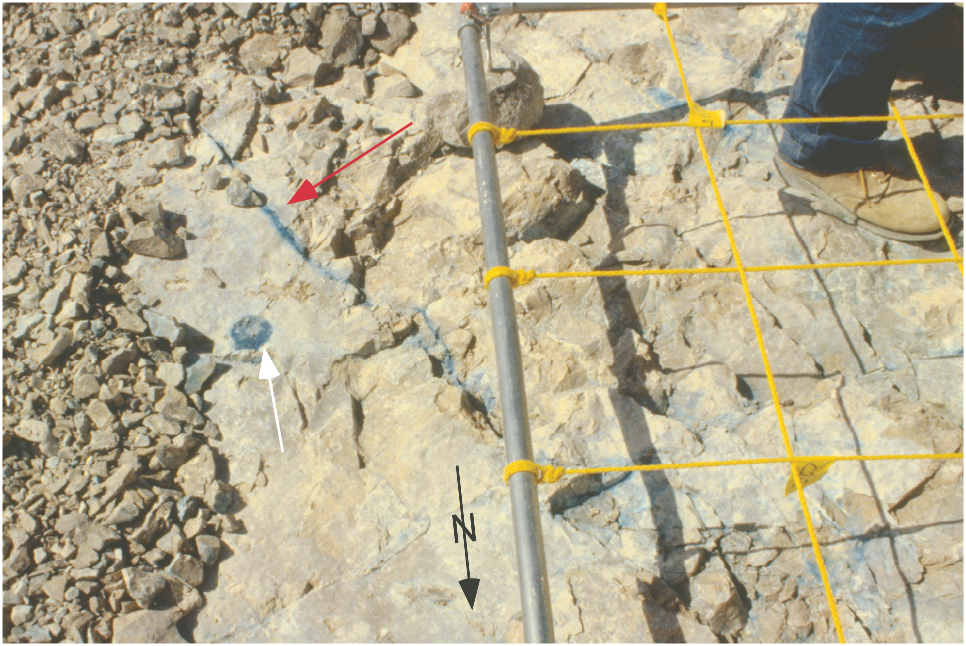

Figure 7.9 - potential impact of instrumentation: Strong tracer stain is seen in a grouted borehole (white arrow) located just east of the restricted flow test at a depth of ~1.5 m below the infiltration surface. This stained borehole was observed at several depths, implying that it acted as a fluid sink and preferential pathway. This observation raises questions regarding perturbations to the flow field resulting from installation of sensing devices. In rock units such as this, where fractures and matrix have extremely different hydraulic properties, use of grout with intermediate properties may significantly impact the flow field and produce non-representative measurements. Also, note that the borehole penetrates a stained subhorizontal pavement surface, and that the pavement is traversed by a vertical fracture carrying flow away from the mapped area (red arrow).

Nicholl and Glass, 2002

Section 8 - Rock Mass Variability

Noting that this was a small excavation, we were still surprised by the degree of variability within the rock mass.

return

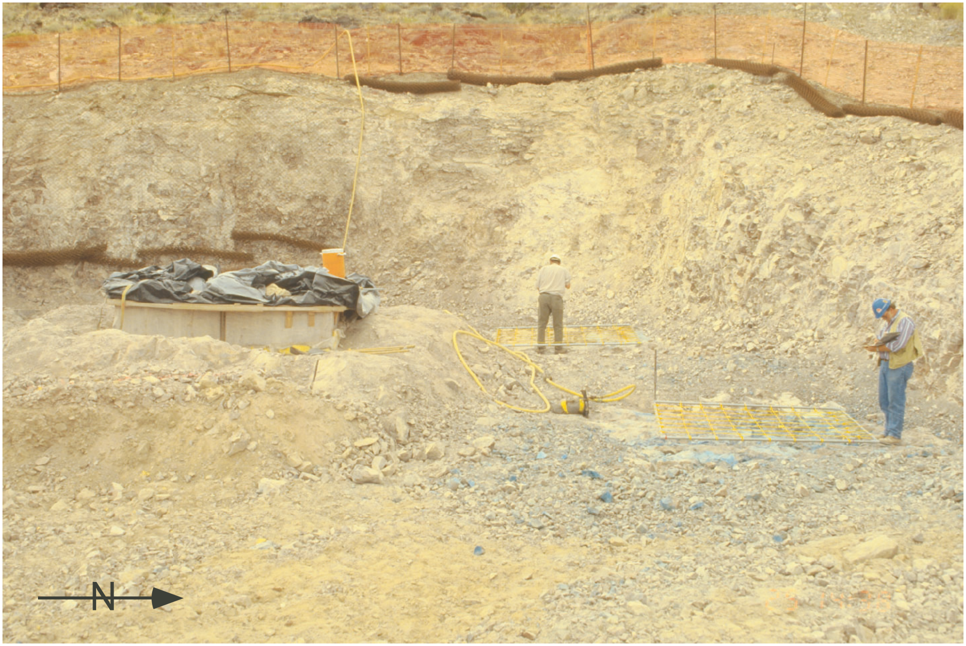

Figure 8.1 - spatial variability of the rock mass: Overview of work site midway through the excavation process; view is looking slightly north of west. In the background, M.J. Nicholl (SNL) is mapping the small slug test, while in the foreground D. Engstrom (SNL) maps the restricted flow test; both tests were located along the north edge of the excavation (see figure 2.5 – site map). Our ponded infiltration test was run in the southwest corner of the excavation; on the far left hand side of this image, and behind the LLNL Large Block (under the black tarp). Note the extreme variability in rock competency within this relatively small area. To the south (left), the densely welded tuff unit is extremely hard and competent; the excavation wall stands vertical, and actually has a slight overhang (see figure 8.4 - extensive fractures). Conversely, the northwest corner (right rear of the image) is highly shattered and weathered. As a result, the rock is friable and will not hold a vertical slope (see figure 8.2 - friable rock). Moving eastward along the north wall (to the right of the mapping grids), the rock becomes more competent, but not nearly so as in the southern half of the excavation.

Nicholl and Glass, 2002

return

Figure 8.2 - friable rock: In the northwest corner of the excavation (see figure 2.5 - site map), the rock mass was shattered and highly weathered; significant amounts of caliche were also present (see also figure 8.1 – spatial variability of the rock mass). Rock in this corner was sufficiently friable to be excavated with a shovel, and would not sustain a vertical excavation; chain link fence was draped across the slope as protection against rock fall. Less than 15 m away, in the southwest corner of the excavation where we performed the ponded infiltration test, the rock mass was extremely hard and relatively impermeable (see figure 8.4 - extensive fractures). Where subsurface materials exhibit such extreme variability in terms of both the matrix and fracture network, prediction of system behavior will be difficult. This observation underscores the complexity of designing appropriate field experiments and conceptual models for flow in unsaturated fractured rock.

return

Figure 8.3 - secondary alteration: In the northwest corner of the excavation (see also figure 8.1 - spatial variability of the rock mass) where we performed the small slug test, portions of the rock mass were highly altered by weathering, and significant amounts of caliche was present. Hydraulic properties of the caliche and weathered rock were intermediate to the unaltered matrix and open fractures. The unaltered matrix is hydrophilic and generates large matrix suction; however, permeability is so low that significant imbibition is precluded. Conversely, the fractures are highly permeable when saturated, but act as capillary barriers when dry. The caliche and weathered zones exhibit hydraulic properties intermediate to these two extremes, hence they act as fluid sinks. In this image, flow was constrained to the weathered and caliche filled portion of the fracture (right hand side).

Nicholl and Glass, 2002

return

Figure 8.4 - extensive fractures: South wall of the excavation adjacent to our ponded infiltration test. Closely spaced, steeply dipping fracture sets are seen to span the full ~5 m depth of the excavation. Note that the excavation is not perpendicular to strike; hence, apparent dip is shallower than true dip. Although wire mesh has been bolted to the wall for protection, this hard competent rock mass easily stands vertically without support.

Nicholl and Glass, 2002

return

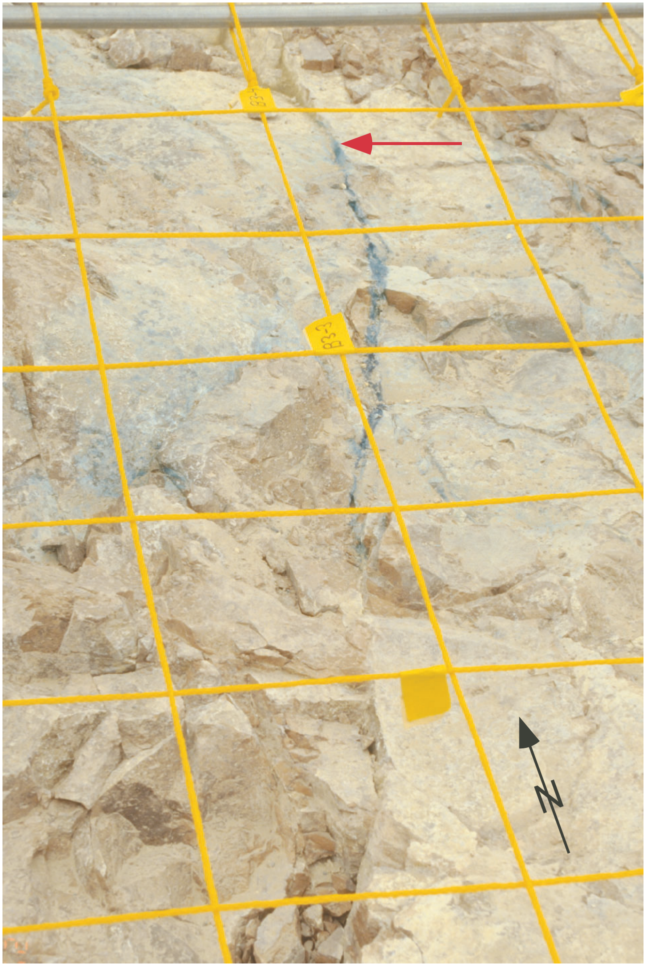

Figure 8.5 - heterogeneity within a fracture: This extensive, near vertical fracture (red arrow) passed through the prism underneath our small slug test at a depth of ~0.5 m beneath the infiltration surface. The mapping grid is subdivided into 0.305 x 0.305 m (1 x 1’) squares. Note that the stain is concentrated in portions of the fracture that are weathered and filled with caliche. Less weathered zones of the fracture (top and bottom of the image) show no evidence of stain. Note also extensive stain on the subhorizontal fracture; smooth undulating surface of this feature suggests cooling, rather than tectonic origin [see Throckmorton et al., 1995].

Nicholl and Glass, 2002

Section 9 - Acknowledgments

This field experiment was designed and data was collected with support from the U.S. Department of Energy, Office of Civilian Radioactive Waste Management, Yucca Mountain Site Characterization Project Office, under contract DE-AC04-94AL85000, WBS 1.2.5.4.6, WA-0040 and WA-0152, and QAGR 1.2.5.4.6 Revision 0; and is contained in SNL YMP controlled scientific notebooks entitled "Infiltration/Flow Path Visualization Test at Fran Ridge (parts 1 and 2)", YMP accession #’s MOL.19961029.0104 and MOL.19961029.0110, respectively. Analysis and interpretation of this data was supported by the U.S. Department of Energy, Basic Energy Sciences Geoscience Research Program under contract numbers DE-FG03-01ER15122 (University of Idaho) and DE-AC04-94AL85000 (Sandia National Laboratories). ERT imagery was designed and executed by B. Daily and A. Ramirez of LLNL. M. Mann (SNL) assisted in the ponded infiltration study. Mapping assistance was provided by D. Engstrom and S. McKenna of SNL. C.A. Rautman (SNL) provided invaluable assistance at putting this work into the proper geologic context, and in facilitating mapping. This work could not have occurred without the assistance of W. Lin and M. Owens of LLNL. The final document was improved significantly through careful review by C.A. Rautman and J. Lorenz, both of SNL.

Section 10 - Guide to Appendices

Folder name	**Contents**
PAPERS	Folder containing other documents relevant to this investigation.
IMAGES	Folder containing high resolution copies of the photographs used in the main document; there are no annotations to these images (arrows, etc.).
PMAPS	Folder containing scanned images of the pavement maps at 300 DPI resolution.
TMAPS	Folder containing high resolution images of the tracer extent maps developed for the ponded infiltration test.
DATA	Contains two files: **FLOW.PDF** contains cumulative outflow data from the feed tank to the infiltration pond, and **NETWORK.PDF** contains fracture data (trace length, orientation) extracted from the pavement maps collected from beneath the ponded infiltration test.

Note 1: Folders containing the appendices are located in a folder entitled APPEND, which may be found on the CD-ROM version of this document.

Note 2: In order to enhance document portability across platforms and between operating systems, the names of all files and folders are in all capital letters, and the main body of each name is no longer than 8 characters (ISO 9660 compatible).

Note 3: Additional details on the information contained within an individual folder may be found in **READ_ME** files located within that folder.

Section 11 - Reference List

Bedinger, M.S., K.A. Sargent, and W.H. Langer, Studies of geology and hydrology in the basin and range province, southwestern United States, for isolation of high-level radioactive waste - Evaluation of the regions, USGS Professional Paper 1370-H, 61 p., 1990.

Call, R.D., J.P. Savely, and D.E. Nicholas, Estimation of joint set characteristics from surface mapping data, Proc. 17th US Symposium on Rock Mechanics, compiled by W.S. Brown, S.J. Green, and W.A. Hustrulid, pp. 2 B2-1-9, Snowbird, Utah, August 25-27, 1976.

Eaton, R.R., C.K. Ho, R.J. Glass, M.J. Nicholl, and B. W. Arnold, Modeling of flow through fractured tuff at Fran Ridge, Proc. 7th Int. Conf. of High Level Rad. Waste Manage., American Nuclear Society, April 29 - May 3, Las Vegas, NV, pp. 76-78, 1996a. [see copy in Appendix]

Eaton, R.R., C.K. Ho, R.J. Glass, M.J. Nicholl, and B.W. Arnold, Three-dimensional modeling of flow through fractured tuff at Fran Ridge, Sandia National Laboratories, Albuquerque, NM, SAND95-1896, 60 pp., 1996b. [see copy in Appendix]

Glass, R.J., M.J. Nicholl, A. L. Ramirez, and W.D. Daily, Phase structure within a fracture network beneath a surface pond: Field experiment, Water Resources Research, 38(10), 1199, doi:10.1029/2000wr000167, 2002. [see copy in Appendix]

Glass, R.J., M.J. Nicholl, and V.C. Tidwell, Challenging models for flow in unsaturated, fractured rock through exploration of small scale flow processes, Geophysical Research Letters, 22(11), 1457-60, 1995. [see copy in Appendix]

Glass, R.J., M.J. Nicholl, M.J., and V.C. Tidwell, Challenging and improving conceptual models for isothermal flow in unsaturated, fractured rock through exploration of small scale processes, Sandia National Laboratories, Albuquerque, NM, SAND95-1824, 61 pp., 1996. [see copy in Appendix]

Reference List (cont.)

Glass, R.J., M.J. Nicholl, and L. Yarrington, Development and experimental evaluation of models for low capillary number two-phase flows in rough walled fractures relevant to natural gradient conditions, Sandia National Laboratories, Albuquerque, NM, SAND96-2820, 116 pp., 1997.

Glass, R.J., M.J. Nicholl, and L. Yarrington, A modified invasion percolation model for low capillary number immiscible displacements in horizontal rough walled fractures: Influence of local in-plane curvature, Water Resources Research, 34(12), 3215-3234, 1998.

Lin, W., Blair, S., Wilder, D., Carlson, W., Wagoner, J., DeLoach, L., Danko, G. Ramirez, A., and K. Lee, Large Block Test Final Report, UCRL-ID-132246, Lawrence Livermore National Laboratory, Livermore, CA, 2001.

Lin, W., D.G. Wilder, J.A. Blink, S.C. Blair, T.A. Buscheck, D.A. Chesnut, W.E. Glassley, K. Lee, and J.J. Roberts, The testing of thermal-mechanical-hydrological-chemical processes using a large block, Proc. of the Fifth Ann. Int. Conf. on High Level Rad. Waste Mgmt., 1938-1945, Am. Nuclear Soc., Las Vegas, Nevada, May 22-26, 1994.

Nicholl, M.J., and R.J. Glass, Effective media models for unsaturated fractured rock: A field experiment, Proceedings of the Sixth Annual International Conference on High Level Radioactive Waste Management, American Nuclear Society, 39-40, Las Vegas, Nevada, May 1-5, 1995. [see copy in Appendix]

Nicholl, M.J., R.J. Glass, and H.A. Nguyen, Small-scale behavior of single gravity-driven fingers in an initially dry fracture, Proc. of the Fourth Ann. Int. Conf. on High Level Rad. Waste Mgmt., 2023-2032, Am. Nuclear Soc., Las Vegas, Nevada, April 26-30, 1993.

Nicholl, M.J., R.J. Glass, and S.W. Wheatcraft, Gravity-Driven infiltration instability in initially dry nonhorizontal fractures, Water Resources Research, 30 (9), 2533-2546, 1994.

Reference List (cont.)

Nicholl, M.J., H. Rajaram, and R.J. Glass, Factors controlling satiated relative permeability in a partially-saturated horizontal fracture, Geophysical Research Letters, 27(3), 393-96, 2000.

Norris, A.E., F.M. Byers, Jr., and T.J. Merson, Fran Ridge horizontal coring summary report, hole UE-25h#1, Yucca Mountain area, Nye County, Nevada, Los Alamos National Laboratory, Los Alamos, N.M., LA-10859-MS, 78 p., 1986.

Rager, A.H., Satellite image of Yucca Mountain Project area, US Department of Energy, Yucca Mountain Site Characterization Project, GIS map product YMP-97-201.0, submitted under activity 8.3.1.4..2, 1997.

Throckmorton, C.K., and E.R. Verbeek, Joint networks in the Tiva Canyon and Topopah Springs tuffs of the Paintbrush Group, southwestern Nevada, USGS Open-File report 95-2, United States Geological Survey, Denver, Colorado, 1995.

Wilder, D.G., W. Lin, S.C. Blair, T. Buscheck, R.C. Carlson, K. Lee, A. Meile, A.L. Ramirez, J.L. Wagoner, and J. Wang, Large Block Test Status Report, UCRL-ID-128776, University of California, Lawrence Livermore National Laboratory, Livermore, California, 1997.

Wagoner, J.L., Fracture Characterization of the Large-Block Test, Fran Ridge, Yucca Mountain, Nevada, UCRL-ID-133846, University of California, Lawrence Livermore National Laboratory, Livermore, California, 1999.

Distribution List

1 Pierre M. Adler
Institut de Physique du Globe de Paris
tour 24, 4, Place Jussieu
75252 Paris Cedex 05 - France

1 David Alumbaugh
University of Wisconsin
1415 Engineering Drive
Madison, WI 53706

1 Randy Bassett
University of Arizona
John W Harshbarger 304d
PO Box 210011
Tucson, AZ 85721

1 Dave Benson
Desert Research Institute
2215 Raggio Parkway
Reno, NV 89512

1 Brian Berkowitz
Weizmann Institute of Science
76100 Rehovot, Israel

1 Stephen Blair
Lawrence Livermore National Laboratory
Mail Stop L-201
7000 E Ave
Livermore, CA 94550

1 Gudmundar Bodvarsson
Lawrence Berkeley National Laboratory
1 Cyclotron Rd. Mail Stop 901116
Berkeley, CA 94720

1 Rob Bowman
New Mexico Institute of Min. and Tech.
Dept of Earth and Environmental Sciences
Socorro NM 87801

1 Stephen Brown
New England Research
331 Olcott Drive Suite L1
White River Jct., VT 05001

1 Tom Buscheck
Lawrence Livermore National Laboratory
Mail Stop L-204
7000 E Ave
Livermore, CA 94550

1 Clay Cooper
Desert Research Institute
2215 Raggio Parkway
Reno, NV 89512

1 Bill Daily
Lawrence Livermore National Laboratory
Mail stop L-130, 7000 E Ave
Livermore, CA 94550

Distribution List

1 Alec Desbarats
Geological Survey of Canada
601 Booth St
Ottawa, ON K1A 0E8 Canada

1 Russ Detwiler
Lawrence Livermore National Laboratory
P.O. Box 808
Livermore, CA 94551-0808

1 Christine Doughty
Lawrence Berkeley National Laboratory
1 Cyclotron Rd. Mail Stop 901116
Berkeley, CA 94720

1 Maria Dragila
Oregon State University
3135 Ag Life Sciences Bldg
Corvallis, OR 97311-4501

1 Derek Elsworth
Penn State Univ
104 Holser Bldg
University Park, PA 16802

1 Jerry Fairley
University of Idaho
Dept of Geological Sciences
Moscow, ID 83844-3022

1 Boris Faybishenko
Lawrence Berkeley National Laboratory
1 Cyclotron Rd. Mail Stop 901116
Berkeley, CA 94720

1 R. Fedors
Southwest Research Institute, CNWRA
6220 Culebra Rd
San Antonio, TX 78238

1 Stefan Finsterle
Lawrence Berkeley National Laboratory
1 Cyclotron Rd. Mail Stop 901116
Berkeley, CA 94720

1 Alan Flint
USGS
Placer Hall WRD
Sacramento, California 95819-6129

1 Lorraine Flint
USGS
Placer Hall WRD
Sacramento, California 95819-6129

1 Hannes Fluhler
Inst Terrestrial Ecology, Soil Physics
Grabenstr 11a
Schlieren, CH-8952
Switzerland

Distribution List

1 Markus Flury
Department of Crop and Soil Sciences
Washington State University
Pullman, WA 99164-6420

1 John Gale
Memorial University of Newfoundland
Dept Earth Science
St Johns, NF A1B 3X5 Canada

1 Shemin Ge
University of Colorado
Department of Geological Sciences
Boulder, CO 80309

1 Glendon Gee
Battelle
Pacific Northwest National Laboratories
PO Box 999/MS K9-33
Richland, WA 99352

1 Ronald Green
Southwest Research Institute, CNWRA
6220 Culebra Rd POB 28510
San Antonio, TX 78228-0510

1 Robert Holt
University of Mississippi
Old Chemistry Room 9
PO Box 1848
University, MS 38677-1848

1 Jan Hopmans
University of California Davis
123 Viehmeyer Hall
Davis, CA 95616

1 Paul Hsieh
USGS
Bldg. 15, Mckelvey Building
Menlo Park, CA 94025

1 Max Hu
Lawrence Berkeley National Laboratory
1 Cyclotron Rd. Mail Stop 901116
Berkeley, CA 94720

1 Dave Hudson
U.S. Department of Energy
Yucca Mountain Site Characterization Office
M/S 423
1551 Hillshire Drive, Suite A
Las Vegas, NV 89134

1 Tissa Illangasekare
Colorado School of Mines
Division Env. Science and Eng.
Golden, CO 80401-1887

1 Walter Illman
121 Trowbridge Hall
Dept Geoscience
Iowa City, IA 52242

Distribution List

1 Karsten Jensen
Building 115
DK 2800
Lyngby, Denmark

1 Wolfgang Kinzelbach
Eidgenossische Tech Hochschule Zurich
Inst Hydromechanik Wasserwirtschaft
Honggerberg Zurich, CH-8093
Switzerland

1 Timothy Kneafsey
Lawrence Berkeley National Laboratory
1 Cyclotron Rd. Mail Stop 901116
Berkeley, CA 94720

1 Rosemary Knight
Mitchel 321
Stanford, CA 94305-2215

1 Joel Koplik
Levich Institute
Steinman Hall, #1M-19
City College of CUNY
140th Street and Convent Avenue
New York, NY 10031

1 B. Kueper
Queens University
99 University Ave.
Kingston, Ontario Canada K7L-3N6

1 Ed Kwicklis
Los Alamos National Laboratory
PO Box 1663
Los Alamos, NM 87545

1 Wunan Lin
Lawrence Livermore National Laboratory
P.O. Box 808
Livermore, CA 94551-0808

1 Hui Hai Liu
Lawrence Berkeley National Laboratory
1 Cyclotron Rd. Mail Stop 901116
Berkeley, CA 94720

1 Jane C.S. Long
University of Nevada, Reno
1664 N Virginia Street
Mail stop 168
Reno, NV 89557

1 William Luth
653 North 63rd Pl
Mesa, AZ 85205

1 Earl Mattson
INEEL
Mail Stop 2107
PO Box 1625
Idaho Falls, ID 83415

Distribution List

1 Alex Mayer
Michigan Technological University
Geological Engineering and Sciences
427 Dow
Houghton, MI 49931

1 Larry McKay
University of Tennessee, Knoxville
Department of Geological Sciences
306 Geological Sciences Building
Knoxville, TN 37996-1410

1 Larry Myer
Lawrence Berkeley National Laboratory
1 Cyclotron Rd. Mail Stop 901116
Berkeley, CA 94720

1 Shlomo Neuman
University of Arizona
John W Harshbarger 250
Tucson, AZ 85721

1 Thomas Nicholson
US NRC
11545 Rockville Pike
MS T-9F31
Rockville, MD 20852-2738

1 John Nimmo
USGS
345 Middlefield RD Mail Stop 421
Menlo Park, CA 94025

1 Dani Or
Utah State University
Ag Science Building Room 140
Utah 84322

1 Peter Persoff
Lawrence Berkeley National Laboratory
1 Cyclotron Rd. Mail Stop 901116
Berkeley, CA 94720

1 Fred Phillips
New Mexico Institute of Min. and Tech.
Dept. of Geosciences
Socorro, NM 87801

1 Karsten Pruess
Lawrence Berkeley National Laboratory
1 Cyclotron Rd. Mail Stop 901116
Berkeley, CA 94720

1 Hari Rajaram
University of Colorado Boulder
Civil Engineering 428UCB
Boulder, CO 80309-0428

1 Abe Ramirez
Lawrence Livermore National Laboratory
P.O. Box 808
Livermore, CA 94551-0808

Distribution List

1 Paul Reimus
Los Alamos National Laboratory
PO Box 1663
Los Alamos, NM 87545

1 Carl Renshaw
Dartmouth College
HB 6105
Hanover, NH 03755

1 Bruce Robinson
Los Alamos National Laboratory
PO Box 1663
Los Alamos, NM 87545

1 Rohit Salve
Lawrence Berkeley National Laboratory
1 Cyclotron Rd. Mail Stop 14-116
Berkeley, CA 94720

1 Jean Schmittbuhl
Equipe de Geophysique
Laboratoire de Geologie UMR 8538
Departement Terre Atmosphere Ocean
Ecole Normale Superieure
24, rue Lhomond
75231 Paris cedex 05 FRANCE

1 John Selker
Oregon State University
240 Gilmore Hall
Corvalis, OR 97331

1 Stephen Silliman
University of Notre Dame
156 Fitzpatrick Hall
Notre Dame, IN 46656

1 Buck Sisson
INEEL
mail stop 2107
PO Box 1625
Idaho Falls, ID 83415

1 Eric Smistad
U.S. Department of Energy
Yucca Mountain Site Characterization Office
M/S 523
1551 Hillshire Drive, Suite A
Las Vegas, NV 89134

1 Robert Smith
University of Idaho
PO Box 50778
Idaho Falls, ID 83405-0778

1 Tammo Steenhuis
Cornell University
Riley-Robb
Ithaca, NY 14853

1 David Stonestrom
USGS
345 Middlesfield RD
Menlo Park, CA 94025

Distribution List

1 Grace Su
USGS
345 Middlefield RD
Menlo Park, CA 94025

1 Ed Sudicky
Univerity of Waterloo
200 Ave. W
Waterloo, Ontario
Canada

1 Tetsu Tokunaga
Lawrence Berkeley National Laboratory
1 Cyclotron Rd. Mail Stop 70-108B
Berkeley, CA 94720

1 Andy Tompson
Lawrence Livermore National Laboratory
P.O. Box 808
Livermore, CA 94551-0808

1 Chin-Fu Tsang
Lawrence Berkeley National Laboratory
1 Cyclotron Rd. Mail Stop 901116
Berkeley, CA 94720

1 Yvonne Tsang
Lawrence Berkeley National Laboratory
1 Cyclotron Rd. Mail Stop 901116
Berkeley, CA 94720

1 Markus Tuller
University of Idaho
Dept. Plant, Soil & Entomological Sciences
Ag Science 113
Moscow, Idaho 83844-2339

1 S.W. Tyler
University of Nevada, Reno
1664 N Virginia St., MS 175
Reno, NV 89557

1 M.T. Van Genuchten
US Salinity Lab
450 W Big Springs Road
Riverside, CA 92507-4617

1 Abe Van Luik
U.S. Department of Energy
Yucca Mountain Site Characterization Office
1551 Hillshire Drive, Suite A
Las Vegas, NV 89134

1 Jiamin Wan
Lawrence Berkeley National Lab.
1 Cyclotron RD 90-1116
Berkeley, CA 94720

1 Ed Weeks
USGS WRD
Denver Federal Ctr
PO Box 25046 MS 413
Lakewood, CO 80225

Distribution List

1 Noam Weisbrod
Oregon State University
Dept BioResource Eng.
Corvallis, Oregon 97331-3906

1 Stephen Wheatcraft
University of Nevada. Reno
Dept Geological Sci. 172
Reno, NV 89557

1 John Wilson
New Mexico Institute Min. and Tech.
Dept Earth and Env. Science
Socorro, NM 87801

1 Paul Witherspoon
1824 Monterey Ave
Berkeley, CA 94707

1 Thomas Wood
INEEL
mail stop 2107
PO Box 1625
Idaho Falls, ID 83415

1 Nick Woodward
US department of Energy
25522 Coltrane Dr
Damascus, MD 20872

1 T-C (Jim) Yeh
University of Arizona
John W Harshbarger 250
PO Box 210011
Tucson, AZ 85721

1 Dongxiao Zhang
Los Alamos National Laboratory
PO Box 1663
Los Alamos, NM 87545

1 Robert Zimmerman
Imperial College
Dept Earth Res. Eng.
London SW7 2BP UK

continued next page

Distribution List

Sandia National Laboratories Personnel

1	MS0701	Davies, Peter B, 6100
1	MS0706	Finley, Ray E, 6100
1	MS0706	Rautman, Christopher A, 6113
1	MS0735	Glass, Robert J., 6115
1	MS0735	Ho, Clifford K, 6115
1	MS0735	Altman, Susan J, 6115
1	MS0735	Tidwell, Vincent C, 6115
1	MS0735	Eliassi, Mehdi, 6115
1	MS0735	McKenna, Sean A , 6115
1	MS0735	Meigs, Lucy C, 6115
1	MS0735	Webb, Erik K , 6115
1	MS0750	Walck, Marianne, 6116
1	MS0751	Costin, Laurence S, 6117
1	MS0750	Westrich, Henry R, 6118
1	MS0750	Lorenz, John, 6118
1	MS0719	Webb, Stephen W, 6131
1	MS0451	Conrad, Stephen, 6515
1	MS0778	Barr, George E,6851
1	MS0776	Arnold, Bill, 6852
1	MS1399	Howard, Clifford L, 6855
1	MS9018	Central Technical Files, 8945-1
2	MS0899	Technical Library, 9616
1	MS0612	Review & Approval Desk, 9612 For DOE/OSTI